Master Thesis

Adhesion improvement of CrN based coatings in automotive applications

carried out for the purpose of obtaining the degree of Dipl.-Ing., submitted at TU Wien, Faculty of Mechanical and Industrial Engineering, by

Thomas Spahn

[redacted]

under the supervision of

Univ. Prof. Dipl.-Ing Dr. mont. Paul Heinz Mayrhofer
Institute of Materials Science and Technology, E308

Univ. Ass. Dipl.-Ing. Dr. techn. Vincent Moraes
Institute of Materials Science and Technology, E308

Vienna, February 2020

Affidavit

I declare in lieu of oath, that I wrote this thesis and performed the associated research myself, using only literature cited in this volume.

City, Date [DD/MM/YYYY] *Signature*

Acknowledgements

I would like to express my sincerest gratitude to Univ. Prof. Dipl.-Ing Dr. mont. Paul Heinz Mayrhofer for giving me the opportunity to write this master thesis and to get a deeper insight in the field of material science.

Furthermore, I want to thank my thesis advisor Univ. Ass. Dipl.-Ing. Dr. techn. Vincent Moraes for his guidance and his patience within this thesis.

I also want to thank Tomasz Wojcik and Philip Kutrowatz for helping me with all the TEM-investigations conducted for this study. Furthermore, I want to thank Daniel Primetzhofer and Eduardo Pitthan Filho.

I would like to thank my parents with all my heart. Without their help and support this work and furthermore, my studies wouldn't be possible.

Last, but not least, I want to thank my wife Silvia for all the encouragement and motivation overall these years, especially when I needed a slight kick in the butt to get things done. You helped me no matter what and have always been there for me whenever I needed you.

Table of Contents

Abstract III
Kurzfassung IV
1 Introduction and Motivation 1
2 Thin Film Deposition and Properties 2
2.1 Physical Vapor Deposition (PVD) 2
2.2 Film Growth 6
2.3 Surface Pre-treatment – Etching 8
2.4 Adhesion of Thin Films 9
3 Structural, Morphological and Chemical Analysis 12
3.1 Scanning Electron Microscopy (SEM) 12
3.2 Transmission Electron Microscopy (TEM) 13
3.3 Energy Dispersive X-Ray Spectroscopy (EDX, EDS) 14
3.4 X-Ray Diffraction (XRD) 15
3.5 Secondary Ion Mass Spectroscopy (SIMS) 16
3.6 Elastic Recoil Detection Analysis (ERDA) 17
3.7 Rutherford Backscattering Spectrometry (RBS) 17
4 Mechanical Analysis 19
4.1 Optical Profilometry 19
4.2 Nanoindentation 20
4.3 Tribometer – Oscillating Wear Test (SRV) 21
4.4 Rockwell (HRC-) Adhesion Test 22
5 Experimental Setup 24
5.1 Coating Optimization 25
5.2 1st Setup – Adhesion Improvement 27
5.3 2nd Setup – Adhesion Improvement 30
5.4 3rd Setup – Adhesion Improvement and Etching Rate Determination 31
5.5 Implantation Depth of Cr 32

6 Results 33
6.1 Coating Properties 33
6.2 Adhesion Improvement 38
6.3 Etching Rate Determination of Cr-Ion Etching 46
6.4 Implantation Depth of Cr 50
7 Summary and Conclusion 59
Bibliography 62

Abstract

Global warming, along with climate change, pose some key challenges in the automotive industry, including social pressure and regulatory requirements. One alternative, to reduce the emission of harmful pollutants, is the optimization of the combustion process, e.g. higher pressures and temperatures during the combustion. One well established way of facing those high demands, is the coating of highly loaded parts with CrN. The excellent wear behavior of CrN, along with a good corrosion resistance, are already highly advanced and the topic of various studies. To further enhance the properties of the thin film, the adhesion properties of the coating on a substrate are of high interest.

This thesis was conducted, to enhance the adhesion properties of CrN coatings on two different steel alloys (later referred to as nitrided and hardened steel due to their surface pre-treatment). To determine a baseline coating for further adhesion experiments, several CrN coatings were deposited and analyzed in terms of mechanical properties (hardness, indentation modulus, residual stresses) and structure. Furthermore, to investigate the influence of the surface pre-treatment of the samples on the adhesion properties, several etching procedures (Ar, N_2, Ar+H_2, Cr^+-ion), with modified BIAS and cathode configurations, were conducted and analyzed using SEM, TEM and HRC-adhesion tests. Since Cr-ion etching proofs to be very promising, the etching rate and the implantation depth of Cr into Si and austenite substrates were determined by ERDA, RBS and SIMS measurements, respectively. Beforehand, a calculation of the theoretical implantation depth, using SRIM, was conducted.

The HRC- adhesion test revealed only excellent adhesion results (HF1) of the coating on the nitrided steel substrates. Overall, the adhesion properties of the coating on the hardened steel substrates were worse than for the nitrided samples. An increase in the applied BIAS potential, as well as synchronizing the BIAS to the cathode signal, results in improved adhesion properties. In contrary, the generation of Cr-ions using a two-cathode configuration, resulted in the existence of surface contaminants at the interface. These contaminants, along with cavities, could also be observed for the samples showing subpar adhesion properties.
The highest etching rate (~46 nm/h) was observed for a Cr-ion etching process, utilizing a combination of Ar and H_2 as a working gas. This high etching rate, results from the combination of sputter etching (Ar) with chemical etching (H_2). In comparison, the other Cr-ion processes

using only Ar as working gas showed etching rates between 12 nm/h (DC-BIAS) and 23 nm/h (synchronized BIAS).

The calculated implantation depth of Cr-ions into Si samples (3.4 nm) is approx. two times higher, than for iron or stainless steel. This implantation in Si samples could be verified using SIMS for Cr-ion etched samples, but a deeper implantation is visible. At a BIAS voltage of -1000 V a net implantation depth of roughly 20 nm could be observed. Furthermore, at -700 V an implantation zone of ~16 nm is visible whereas for -300 V a net deposition of a ~150 nm thick Cr layer is detected. ERDA measurements of austenite samples also revealed a net deposition of the etched samples with -300 V and -700 V BIAS of 115 nm and 24 nm, respectively. At -1000 V an ~17 nm thick implantation zone is observed. These results were verified by RBS and TEM analyses.

These findings show, that even advanced coating systems can be further enhanced by applying the proper surface pre-treatment method. Especially Cr-ion etching has the potential to improve the adhesion of the coating and should be further investigated.

Kurzfassung

Der Klimawandel stellt die Autoindustrie vor einige Herausforderungen, dazu gehören sozialer Druck durch die Öffentlichkeit und rechtliche Rahmenbedingungen. Ein Weg, um die Emission von Treibhausgasen zu reduzieren, ist die Optimierung des Verbrennungsprozesses, z.B. durch höhere Drücke und Temperaturen während der Verbrennung. Um den gesteigerten Anforderungen zu genügen, werden hoch beanspruchte Teile häufig mit CrN beschichtet. Das exzellente Verschleißverhalten von CrN, kombiniert mit sehr guten Korrosionseigenschaften, sind bereits sehr ausgereift und das Thema vieler Studien. Für eine weitere Verbesserung der Schichteigenschaften ist das Adhäsionsverhalten der Schicht auf dem Substrat von großem Interesse.

Diese Arbeit beschäftigt sich mit der Verbesserung der Hafteigenschaften von CrN Beschichtungen auf unterschiedlichen Stahlproben (weiters als gehärteter/nitrierter Stahl bezeichnet aufgrund seiner Vorbehandlung). Um eine Ausgangsbasis für die nachfolgenden Haftexperimente festzulegen, wurden mehrere CrN-Schichten abgeschieden und auf ihre mechanischen (Härte, Elastizitätsmodul, Eigenspannungen) und strukturellen Eigenschaften geprüft. Um den Einfluss der Oberflächenvorbehandlung auf die Hafteigenschaften zu bestimmen, wurden diverse Ätzverfahren (Ar, N_2, Ar+H_2, Cr-Ionen), mit modifizierten BIAS- und Kathodenkonfigurationen, getestet und analysiert mittels SEM, TEM und HRC-

Adhäsionstests. Weiters wurden von den Cr-Ionen Ätzversuchen die Ätzrate und die Implantationstiefe von Cr-Atomen in die Oberfläche von Silizium- und Austenitsubstraten mittels ERDA-, RBS- bzw. SIMS Untersuchungen bestimmt. Zuvor wurde bereits eine theoretische Berechnung der Implantationstiefe mittels SRIM durchgeführt.

Die Ergebnisse des HRC-Haftversuches zeigten nur exzellente Hafteigenschaften (HF1) der Schicht auf den nitrierten Stahlproben. Insgesamt wurde eine bessere Adhäsion der Schicht auf den nitrierten Stahlproben als auf den gehärteten Proben beobachtet. Dabei haben Experimente ergeben, dass eine Erhöhung der BIAS-Spannung, sowie eine Synchronisierung des BIAS-Signales zum HiPIMS-Signal, eine Verbesserung der Haftung zur Folge hat. Dem gegenüber steht eine Verschlechterung der Adhäsion, wenn für die Erzeugung der Cr-Ionen zwei Kathoden verwendet wurden. Bei den Proben mit schlechten Hafteigenschaften konnten Oberflächenverunreinigungen und Hohlräume an der Grenzfläche Schicht/Substrat festgestellt werden.
Die höchsten Ätzraten (bis 46nm/h) wurden bei den Cr-Ionen Ätzverfahren festgestellt, bei welchem eine Kombination aus Ar und H_2 als Arbeitsgas verwendet wurden. Diese folgt aus der Kombination von physikalischem (Ar) und chemischem Ätzen (H_2). Die Cr-Ionen Ätzverfahren, bei welchen nur Argon verwendet wurden, erreichten Ätzraten zwischen 12 nm/h (DC-BIAS) und 23 nm/h (synchronisierter BIAS).
Die berechneten Implantationstiefen von Cr in Si (3.4nm) ist um das Doppelte über jenen für Eisen oder Edelstahl. Diese Implantation in die Oberfläche der Siliziumproben konnte durch SIMS-Untersuchungen bestätigt werden, jedoch wurden größere Werte beobachtet. BIAS-Spannungen von -1000 V und -700 V liefern Implantationstiefen von ca. 20 nm bzw. 16 nm. Bei -300 V wurde eine Abscheidung von Cr auf der Probenoberfläche mit einer Dicke von ca. 150 nm festgestellt. ERDA-Messungen von Austenitproben, Cr-Ionen geätzt bei -300 V und -700 V, zeigten ebenso eine Nettobeschichtung der Substratoberfläche mit einer 115 nm bzw. 24 nm dicken Cr-Schicht. Bei -1000 V konnte eine ca. 17 nm tiefe Implantationszone beobachtet werden. Diese Ergebnisse wurden mittels RBS- und TEM-Untersuchungen verifiziert.

Dies Resultate zeigen deutlich, dass sogar bereits sehr ausgereifte Beschichtungssysteme wie CrN, durch den Einsatz der geeigneten Oberflächenvorbehandlung, weiter optimiert werden können. Besonders Cr-Ionen Ätzen hat das Potential das Haftverhalten von Schichten zu verbessern und sollte durch weitere Untersuchung analysiert werden.

List of Figures

Figure 2-1: Schematic sputter deposition process [11]. 3
Figure 2-2: Schematics of magnetron sputtering with permanent magnets. 4
Figure 2-3: Schematics of a HiPIMS signal. 5
Figure 2-4: Structure zone model by Anders [19]. 6
Figure 2-5: Growth mechanisms of films a) Volmer-Weber, b) Frank van der Merwe, c) Stanski-Kastranow. 7
Figure 2-6: Interface regions. 10
Figure 3-1: Pear-shaped interaction volume of electron beam and sample. 12
Figure 3-2: Schematics of the diffraction of electromagnetic waves on atomic lattice planes – Bragg's Law. 15
Figure 3-3: Schematic collision cascade of SIMS. 16
Figure 3-4: Schematic geometry of ERDA. 17
Figure 3-5: Schematic illustration of ion interaction of RBS with corresponding graph of the intensity over the energy of the backscattered ions. 18
Figure 4-1: Schematic profilometry measurement of a) surface topography, b) curvature of substrate (compressive stresses). 19
Figure 4-2: Bending of the specimen due to a) compressive stresses, b) tensile stresses. 20
Figure 4-3:Typical load/displacement curve during nanoindentation [50]. 20
Figure 4-4: Berkovich indenter a) SEM image of the indenter, b) indenter geometry [48]. 21
Figure 4-5: Schematically illustration of a SRV-test. 21
Figure 4-6: Classification categories HF1-HF6 after VDI 3198 [52]. 22
Figure 5-1: Illustration of a coated valve piece. 24
Figure 5-2: "Noreia" deposition plant [54]. 25
Figure 5-3: Desired coating structure. 26
Figure 5-4: Illustration of the used substrate holder a) bottom-up view, b) top-down view. 27
Figure 5-5: Schematic of the target-shutter-substrate configuration with the predicted trajectories for the Cr^{+}- ions and the neutral Cr-atoms, respectively. 29
Figure 5-6: Schematic illustration of the substrates for the etching rate determination. 32
Figure 6-1: XRD-measurements in Bragg-Brentano configuration of CrN coatings at 200 °C with N_2:Ar ration of a) 75:25, b) 80:20 and at 300 °C with N_2:Ar ratio of c) 75:25, d) 80:20. The standardized peak positions for c-CrN, h-Cr and h-Cr_2N are indicated by yellow star, red

cubic, and green hexagonal symbols, respectively. Furthermore, the measurements for coatings deposited using a substrate bias of floating potential, -50 V, and -100 V are displayed in a)-d) from bottom to top..... 33
Figure 6-2: Cross-sectional images of CrN coatings deposited at 200 °C and 300°C, N_2:Ar ration of 80:20 and different BIAS potentials a) b) floating BIAS, c) d) -50 V BIAS, e) f) -100 V BIAS. 35
Figure 6-3: Hardness and residual stresses of the CrN coatings depending on the applied BIAS potential during the deposition process. 36
Figure 6-4: Delamination of the CrN at the 1st experimental setup for a) argon etching at -400 V BIAS, b) Cr-ion etching at -700 V BIAS. 38
Figure 6-5: Results of the HRC-adhesion test for Cr^+-ion etching using different BIAS and cathode configurations. 40
Figure 6-6: Results of the HRC-adhesion test for etching procedures using different BIAS configurations for forming gas, argon and N_2. 41
Figure 6-7: Image of Ar etched nitrided steel sample with a BIAS potential of -1000 V, with the corresponding SAED pattern of the Cr-interlayer and CrN coating. 43
Figure 6-8: Images of the interface, recorded using TEM, of different etched samples at -1000 V BIAS a) hardened steel Ar-etched, b) nitrided steel Ar-etched at, c) hardened steel Cr-ion etched DC BIAS, d) nitrided steel Cr-ion etched DC BIAS, e) hardened steel Cr-ion etched 2 cathodes and DC BIAS, f) hardened steel Cr-ion etched synchronized BIAS..... 44
Figure 6-9: a) Cross-sectional image of an Ar-etched hardened steel sample with the indicated line and orientation of the EDS-line-scan and b) the corresponding result of the at.-% of the observed elements versus distance. 45
Figure 6-10: Cross-sectional images of the masked samples after Cr-ion etching using a gas mixture of Ar/H_2 and coating with Cr interlayer and CrN on a) silicon substrate, with detail of the etched height, b) austenite substrate. 46
Figure 6-11: Measured step height after coating and etching for Cr-ion etching process using forming gas. 47
Figure 6-12: Etching rate for different Cr-ion signal etching procedures for silicon and austenite substrates utilizing argon (Ar) or forming gas (FG = $Ar+H_2$) as working gas (WG). 48
Figure 6-13: Theoretical implantation depth of Cr and Ar ions, calculated using SRIM, in silicon (Si), iron (Fe) and stainless steel (SS) substrates. 51
Figure 6-14: Results of the RBS measurement of a Cr^+-ion etched austenite sample at -300 V applied BIAS potential for impinging angles of a) 5°, b) 40° and c) 60°. d) shows the affiliated

cross-sectional image acquired by TEM. The position of the edges of the signal are linked to the cross-sectional image by ocher lines for Cr and blue lines for Mo, respectively..... 52
Figure 6-15: Graphs of the atomic content versus the depth, of Cr^+-ion etched austenite samples, gained by ERDA. investigations for different applied BIAS potentials a) - 1000 V, b) -700 V and c) -300 V. For -300 V and -700 V the thickness of the deposited Cr-layer is indicated. .. 54
Figure 6-16: Detail of the 1st derivative of the Cr^+-ion etched austenite sample at -1000 V. The presumed implantation zone of Cr-ions into the surface is indicated. 54
Figure 6-17: SIMS-measurements of the intensity versus the sputtering time of Cr^+-ion etched silicon substrates at BIAS potentials of a) -1000 V, b) -700 V and c) -300 V..... 56
Figure 6-18: 1st derivative of the SIMS-measurements illustrated in Figure 6-17 of Cr^+-ion etched silicon substrates at BIAS potentials of a) -1000 V, b) -700 V and c) -300 V. 57
Figure 6-19: Cross-sectional image obtained by TEM of a Cr^+-ion etched Si-sample at an applied BIAS potential of - 300 V. 58

List of Tables

Table 5-1: Coating parameters for the coating optimization testing series 27
Table 5-2: Parameter table adhesion improvement 1st experimental setup 28
Table 5-3: HiPIMS parameter for Cr-ion etching 28
Table 5-4: Parameter table adhesion improvement 2nd experimental series 30
Table 5-5: Parameter table adhesion improvement 3rd experimental setup 31
Table 5-6: Parameter table determination of the implantation depth of Cr 32
Table 6-1: Thickness of the different layers of austenite etched samples at -300 V, -700 V and -1000 V BIAS 53

List of Abbreviations

ABS	Arc bond sputtering
AE	Auger electrons
approx.	approximately
BF	Bright field
BSE	Backscattered electrons
CCD	Charge-coupled device
Cr_2N	Dichromium nitride
CrN	Chromium nitride
CTEM	Conventional transmission electron microscopy
DC	Direct current
DF	Dark field
e.g.	for example
EDS, EDX	Energy-dispersive X-ray spectroscopy
EELS	Electron energy loss spectroscopy
ERDA	Elastic recoil detection analysis
FIB	Focused ion beam
FG	Forming gas
HAADF	High angle annular dark field
HB	Hardness according to Brinell
HiPIMS	High power impulse magnetron sputtering
HR(C)	Hardness according to Rockwell (Cone)
HRTEM	High resolution transmission electron microscopy
HV	Hardness according to Vickers
i.e.	that is
LED	Light emitting diode
M	Metal atoms
PDF	Powder diffraction file
PVD	Physical vapor deposition
RBS	Rutherford backscattering spectrometry
RF	Radio frequency
SAED	Selected area electron diffraction

SE	.....	Secondary electrons
SEM	.....	Scanning electron microscopy
SIMS	.....	Secondary ion mass spectrometry
SRV	.....	Oscillating wear test
SS	.....	Stainless steel
STEM	.....	Scanning transmission electron microscopy
SZM	.....	Structure zone model
TEM	.....	Transmission electron microscopy
TiO_2	.....	Titanium dioxide
UHV	.....	Ultra-high vacuum
VDI	.....	Verein Deutscher Ingenieure
WG	.....	Working gas
XRD	.....	X-ray powder diffraction

1 Introduction and Motivation

Global warming, along with climate change, are today's key challenges, the automotive industry must face. Road transport, including light or heavy duty vehicles and non-road mobile machinery, is accounted for around 15 % of the CO_2 emissions in Europe [1]. Therefore, the automotive sector faces increasing social pressure and regulatory requirements. One way, to face those challenges, is to optimize the combustion process of diesel and petrol engines [2]. Higher pressures and temperatures, during the combustion, are key factors to reduce harmful emissions, thus putting higher demands on the used materials. For example, during the fuel injection, pressure values of more than 2000 bar in the injection valve are common nowadays.

A well-established way to meet those requirements for high pressures and cycles, is the deposition of thin ceramic coatings onto heavily loaded components. In the automotive industry, nitride-based coatings are commonly used to protect high precision components, e.g. the mentioned high-pressure injection valves. Due to their high hardness, good corrosion resistance along with excellent wear behaviour, chromium nitride (CrN) based thin films are the material of choice in this application [3].

The tribological and mechanical properties of CrN coatings are already the topic of various studies and therefore highly advanced. To further enhance the application range of such films this thesis was conducted, focusing on enhancing the adhesion properties of the coating onto various commonly used steel substrates in the automotive industry.

The first conducted experimental series focuses on the optimization of the CrN coating, which will act as a baseline for further adhesion characterization. In the second step, to enhance the adhesion of the coating on the substrate, various etching procedures (Ar, N_2, Ar/H_2 and Cr-Ion), prior to the coating process, are investigated. Their influence on the interface of the substrate and coating, as well as the adhesion properties were examined and compared. To get an insight about the etching process itself, the etching rates were determined. Furthermore, investigations for the metal ion etching processes were conducted, regarding the implantation of Cr^+-ions into the substrate.

2 Thin Film Deposition and Properties

The requirements on materials are vastly improving and the development of bulk materials alone is no longer sufficient. One alternative — to improve the properties of components — is the modification of the surface. The combination of characteristics from the bulk material and applied surface modification allows for a large array of parameter sets. One example is the high ductility of a bulk material combined with the high hardness of the thin film [4]. Many different surface modification methods are usually in use, which can be categorized into the conversion of the surface and the deposition of films. As the name implies, for conversion, the surface of the component itself undergoes a modification process. Examples are the formation of nitrides and carbides of the substrate material in surface near regions through nitriding and carburizing, respectively [5].

The second category is the deposition of coatings. A thin film is deposited onto the substrate material to alter the properties of the surface in a desired manner [6]. Depending on the application and the coating material, many different deposition techniques are in use. One very powerful method, in the aspect of versatility of the gained properties of the coating, is the formation of thin films through physical vapor deposition (PVD). For coatings, produced by PVD, the typical thickness is in the range of a few nanometres up to 10 µm, but even monolayered films can be deposited. However, the mechanical properties can be increased in the range of one or two order of magnitudes (e.g. hardness values of 40 GPa and more are possible) [7].

2.1 Physical Vapor Deposition (PVD)

Physical vapor deposition can be characterized as an atomic deposition process, meaning the coating material deposits atom-by-atom. A typical PVD-process can be described by 3 main steps [7]:

- Evaporation of the target material.
- Transport of the vaporized material from the target to the substrate.
- Condensation of the vaporized material onto the substrate, nucleation and film growth.

In general, the process takes place in a vacuum chamber, to maximize the mean-free path of the evaporated target material, as well as to minimize the contamination of the deposited film. Furthermore, it is possible to deposit compounds, such as nitrides, or carbides, by applying a

reactive gas atmosphere, so-called reactive physical vapor deposition. The vaporized target material interacts with the gaseous environment, allowing the deposition of a film with different chemical composition than the target material. This interaction mostly takes place at the surface of the target or the substrate. Thus, a coating can be formed on the target itself, leading to changed process conditions. This phenomenon is referred to as “target poisoning” and should be minimized or avoided. Therefore, the reactive gas inlet is commonly placed near the substrate [8].

The different PVD-techniques are distinguished by the physical evaporation possibilities of the target material, such as thermal (vacuum) evaporation, sputter deposition, cathodic arc evaporation, or ion plating. The used evaporation method does not only affect the entire process but also the thin film itself. For example, the deposition rates of arc evaporation are higher (up to 25 times) than for sputtering, due to the higher ionization degree of the target material [7,9].

2.1.1 (Magnetron-) Sputtering

Sputter deposition is based on the vaporization of material through momentum transfer. Therefore, high energy ions (e.g. Ar^+ or N^+) are accelerated (by an applied voltage) and bombard the target surface, leading to the backward scattering of surface near atoms or clusters of the target material. This process is called “back-sputtering” or simply “sputtering”. Other phenomena may occur besides the ejection of surface near atoms, like the implantation of the impinging ions or the reflection as a high energetic neutron. Furthermore, 95% of the energy of the incoming ions dissipates in the surface near region of the target material. A parameter for the efficiency of the sputtering process is the so-called “sputtering yield”. It is defined as the ratio of the ejected target atoms per impinging ion and is highly dependent on the target material, the species of bombarding ion and their energy, and their angle of incidence [10]

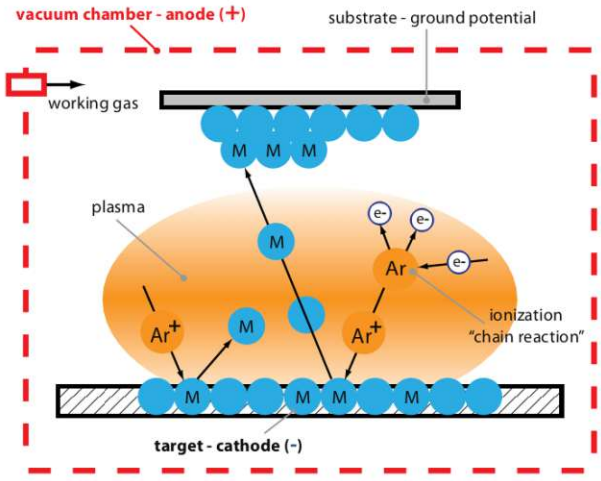

Figure 2-1: Schematic sputter deposition process [11].

The most common application of sputtering is plasma-based sputtering. A plasma is defined as an ionized gas, with an equal number of co-existing positive and negative charged particles (ions and electrons). Figure 2-1 illustrates such a sputtering process. The working gas (commonly Argon), is ionized by glow discharge. Due to a potential drop between the plasma and the target surface (cathode), the Ar^+ ions are accelerated towards the cathode, leading to the ejection of target atoms or clusters, e.g. metal atoms (M). These atoms move through the vacuum chamber and condense on the substrate surface and subsequently forming a thin film.

The simplest way, to obtain a glow discharge, is by the application of a DC (direct current) potential between the electrodes of the system. The plasma is generated near the cathode surface, in the negative glow region. Disadvantages are the low deposition rates, the high voltages needed to achieve the glow discharge, relatively high working gas pressures and the limitation to conductive target materials. For non-conductive materials a RF (radio frequency)-field is applied to the target. In the most used systems, a frequency of 13.56 MHz is used. RF sputtering also results in low deposition rates [12].

In conventional DC sputtering, the exited electrons form the cathode do not sufficiently contribute to sustain the discharge. One way to overcome this problem is the application of a magnetic field near the target surface. The electrons are “trapped” and circulate on closed trajectories, thus creating a high-density plasma close to the cathode, see Figure 2-2. With this magnetron sputtering configuration, higher sputter yields, compared to RF or DC, are obtained, while simultaneously giving the possibility of lowering the pressure of the working gas and reduce the applied potentials. Different magnetron arrangements are used in deposition plants, e.g. (commonly used) planar magnetrons, cylindrical and circular. The magnetic field can be produced using permanent magnets, electromagnets, or the combination of both. One disadvantage is the variation of the plasma density over the target surface, leading to non-

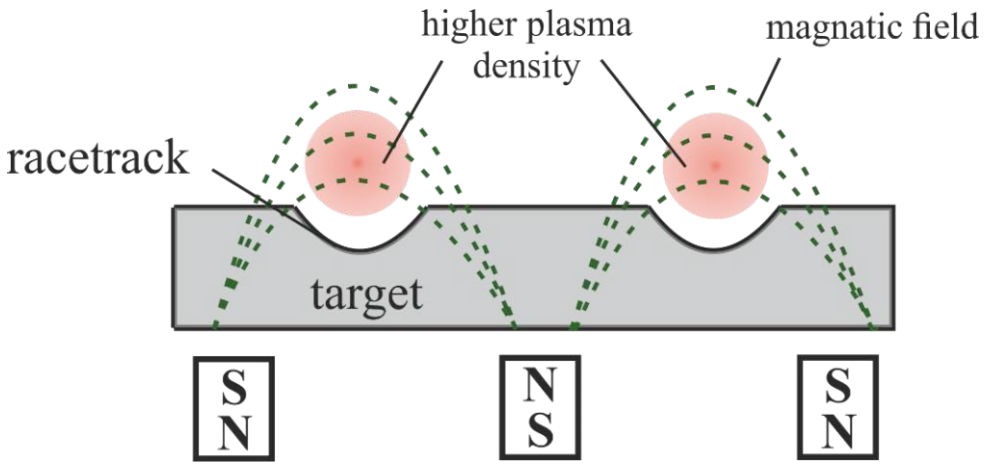

Figure 2-2: Schematics of magnetron sputtering with permanent magnets.

uniform sputtering of the target. This area of non-uniform erosion is called racetrack. The utilization of the target can be as low as only 10% of the target material is used before it is recycled [7,13].

When the inner and outer magnet have the same strength, the system is referred to as balanced magnetron sputtering. The magnetic field lines loop between the magnetic setup, therefore the plasma is confined near the cathode. To activate reactive gases or to improve diffusion processes at the substrate, through ion bombardment during deposition, a plasma is needed near the substrate. This can be achieved by an unbalanced magnetron configuration, where the inner or the outer magnet is stronger than the other, leading to non-looped field lines. Some secondary electrons are now able to escape the magnetic field, contributing to ion formation near the substrate surface [7].

2.1.2 High Power Impulse Magnetron Sputtering (HiPIMS)

In conventional DC magnetron sputtering deposition plants the ionization of the ejected target material is very low (1 or 2%) and are trapped near the cathode surface. Therefore, they are not contributing to the formation of the coating [14]. Studies indicated [15], that the bombardment of ions during the deposition process is beneficial to the thin film properties. To obtain such a steady impingement of ions, higher degrees of ionization are desired, thus leading to the development of ionized PVD, such as HiPIMS. Using HiPIMS, ionization degrees of the target material of 30 to almost 100% can be achieved, depending on the target material and process parameters. This ion flux is used for a controlled ion bombardment, by an acceleration of the ions, due to a negative bias potential applied to the substrate [14].

High power impulse magnetron sputtering utilizes high peak voltages (U_{peak}) and currents (I_{peak}), only applied at short durations (t_{on}), to ionize the ejected target material, see Figure 2-3. Typically, peak voltages in the range of 500-2000 V and peak current densities of 3-4 A/cm^2, with repetition frequencies of 50-5000 Hz are used for the HiPIMS discharge, resulting in peak power densities of 0.5 to 10 kW/cm^2. The average power ($P_{average}$) over the whole cycle is nearly

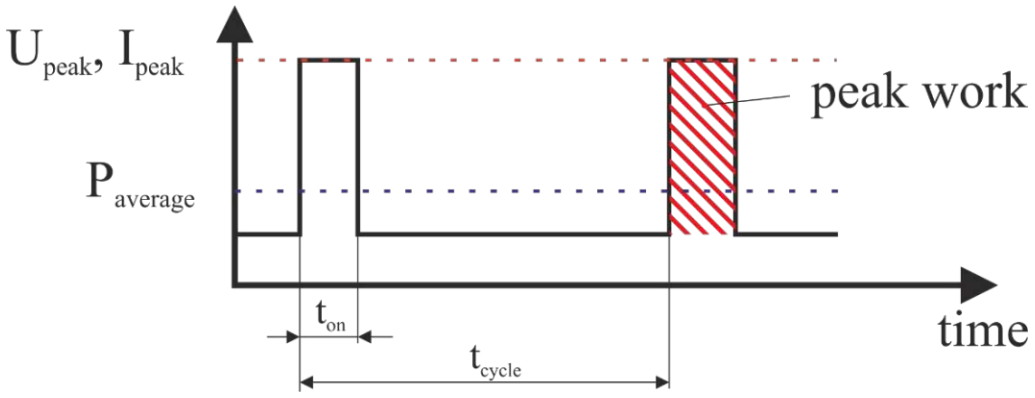

Figure 2-3: Schematics of a HiPIMS signal.

the same as for DC magnetron systems, due to the short duty cycles (0.5-5%, ratio of t_{on} to t_{cycle}) of the applied signals [16].

As mentioned, an ion bombardment of the substrate during deposition is beneficial to the coating properties, such as higher densities, higher hardness, improved surface roughness and adhesion of the film. Furthermore, during the on-time of the signal, the instant deposition rates reaches high levels, resulting in an immense amount of adatoms on the substrate surface. This changes the growth conditions of the coating, leading to flat surfaces and dense microstructures, even for relative complex geometries. The deposition rates for HiPIMS are usually lower than for conventional DC magnetron sputtering [16,17].

2.2 Film Growth

The morphology and crystallinity of a thin film highly influence the properties of a coating. Therefore, controlling the grain and column size in a desired manner is of high importance during a coating process. To easily describe the growth mode of a PVD deposited film, so-called structure zone models (SZM) are developed. The first SZM has been already introduced 1969 by Movchan and Demchishin [18], with the goal to predict the morphology of a thin film, depending on as few influencing parameters as possible. In the case of Movchan and Demchishin, the growth of the coating only depends on a so-called homologous temperature (ratio of the substrate temperature during the deposition process and the melting temperature of

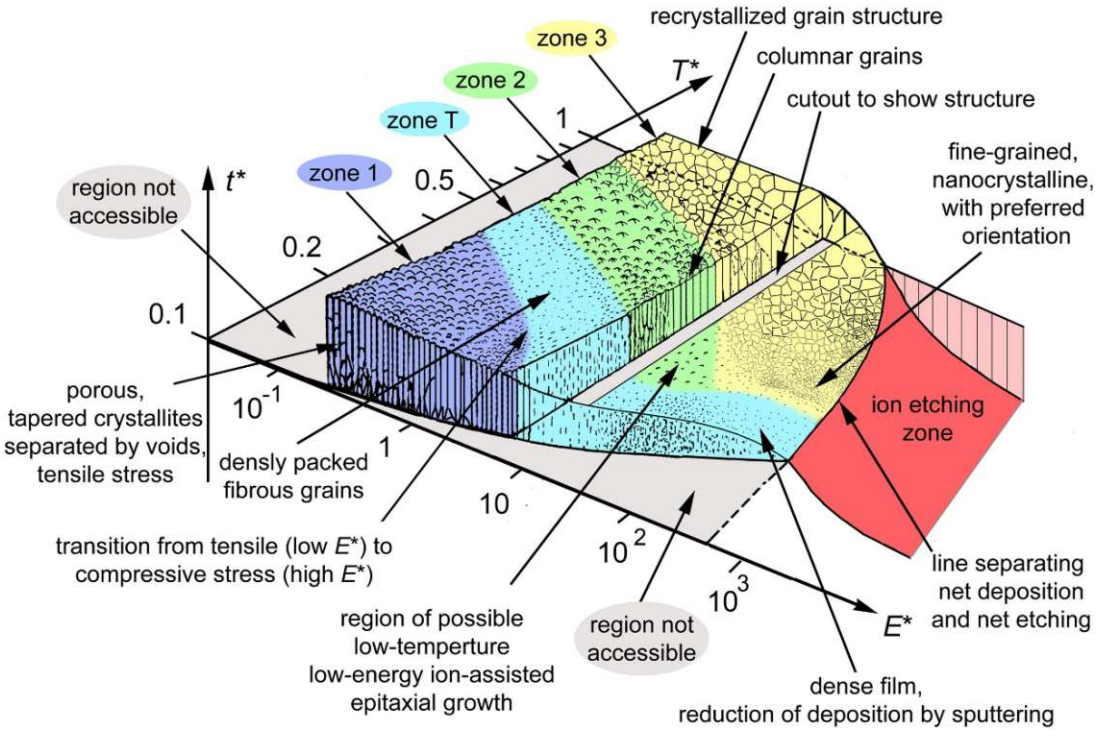

Figure 2-4: Structure zone model by Anders [19].

the target material). Due to the advancement in PVD-processes, more refined models were developed, leading to the generally accepted SZM by Anders [19].

The SZM by Anders, Figure 2-4, categorises the crystallite growth and their resulting grain structure into 4 different zones (zone 1, T, 2, 3). The obtained growth mode depends on the normalized temperature T^*, the normalized energy E^* (considers heating and displacement effects) and the net film thickness t^*. The normalized temperature T^* is, similar to Movchan and Demchishin, a ratio of the film growth temperature and the melting temperature of the deposited material. T^* also includes a temperature shift, due to the potential energy of arriving atoms to the substrate during deposition. The net thickness t^* can reach negative values, caused by sputtering, densification of the film, or ion etching [19].

The mentioned structure zone models describe the film growth only depending on a few influencing parameters, whereas in reality, it is a highly complex phenomenon. The film growth takes place in stages. At first, the target atoms or clusters impinge on the surface of the substrate and are either reflected, or they transfer enough energy to loosely bond to the substrate surface, as so-called adatoms. The adatoms then diffuse on the surface until they form a stable nucleus, condense on already formed nuclei, or desorb from the surface. The formation of stable nuclei if only possible, if a certain critical nucleus radius is reached. To describe their development, different models are in use, e.g. “droplet-model” and “particle-model”. The primary formed nuclei grow until they encounter each other and coalescence (grow together). They form island on the substrate surface. After initial nucleation, further target atoms absorb onto the surface, so-called secondary nucleation. These secondary adatoms fill the holes, left by the primary nucleation, until a continuous film is formed [7]. Three growth modes are distinguished, Figure 2-5. Three-dimensional growth, the so-called Volmer-Weber growth, is present, if the adatoms are more easily bonded to each other than the substrate. Monolayer by monolayer growth, or 2D Frank van der Merwe, occurs, when the bonding of the coating atoms is stronger to the substrate than to each other. Various modes exists within (as a mixture of the previous discussed), which are summarized as Stranski-Kastranow mechanism [12].

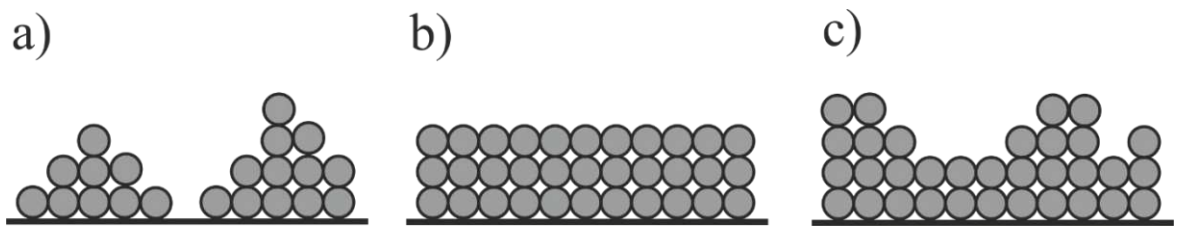

Figure 2-5: Growth mechanisms of films a) Volmer-Weber, b) Frank van der Merwe, c) Stanski-Kastranow.

2.3 Surface Pre-treatment – Etching

To achieve optimized and desired coating properties the pre-treatment of the surface is essential. The preparation of the surface can be done through cleaning or altering the surface in a certain manner. Some surface pre-treatment procedures achieve both.

Unwanted contaminants, influencing the growth and the adhesion of the thin film, have to be removed prior to the deposition process. Surface contaminants can be classified as reaction layers (e.g. oxide, carbide layers), adsorbed layers (e.g. hydro carbides – from corrosion inhibitors), variable composition contaminants, or particulate contaminants (dust). Generally, cleaning procedures result in the removal of surface material along with the contaminants. For the application in PVD, the cleaning process is typically divided into external cleaning (exterior to the deposition plant) and internal cleaning (in the deposition plant, normally right before the coating process). Both, internal and external cleaning, are usually performed prior to the deposition process. A standard external cleaning process for PVD is the ultrasonic cleaning in a solvent bath [7].

One of the most used internal cleaning techniques in PVD, and also applied during this thesis, is the sputter-etching. The principles are the same as used in sputtering for the ejection of the target material during the deposition process, see chapter 2.1.1. A plasma is created in the vacuum chamber by glow discharge. During sputter etching, a negative potential is applied to the substrate, thus accelerating the Ar^+ ions towards it. Therefore, the outermost surface layers of the substrate are removed, along with the contaminants. A disadvantage of this procedures, is that the implantation of gas atoms may occur, resulting in poor adhesion of the coating [20].

Reactive sputter etching (also referred to as reactive ion etching) is a more advanced sputter etching technique. Instead of a non-reactive gas alone, a mixture of noble gas (mostly Ar) and reactive gas (e.g. H_2) is used. The concentration of the reactive gas is mostly in the range of 1-10 vol.-%. In reactive plasma etching, two mechanism contribute to the etching rate, the removing of material through sputtering (high energetic ions) and chemical etching (thermic induced radical formation of the reactive gas). For reactive sputter-cleaning the etching rates are higher compared to conventional sputter cleaning [21,22].

2.3.1 Metal Ion Etching

Conventional sputter etching uses non-reactive noble gases to clean the outermost surface of the substrate, whereas metal ion etching mainly utilizes ionized metal atoms (along with ions from the working gas) for the etching procedure. These metal ions can be produced through cathodic arc discharge, leading to the development of the arc bond sputtering (ABS) technique.

Another alternative of producing the needed metal ion flux is HiPIMS, which removes the problem of the droplet formation present with ABS. To guide and accelerate the created ions, a negative bias potential is applied to the substrate. With metal ion etching, higher etching rates and cleaner surfaces can be obtained than for sputter etching using noble gases like Ar, due to the higher mass and energy of the ions. The removal of oxide or carbide layers proof to be more sufficient with metal ion etching. However, the biggest advantage, is the improved adhesion of the coatings onto the substrate. Due to the bombardment with the high energetic metal ions, an alteration of the surface takes place. Impinging metal ions are implanted into the substrate surface, leading to the development of a pseudo-diffusion-zone. Consequently, an adherent interface between the substrate and the coating is developed. Furthermore, depending on the substrate bias (therefore the kinetic energy of the impinging ions) the formation of an amorphous interlayer has been observed [23,24].

Many different metals have already been utilized for metal ion etching, e.g. Cr or Nb for CrN [24,25], Cr or Ti for DLC [26] and V for TiAlCN/VCN multilayer coatings [27]. Strongly depending on the used metal atom, the bias potential applied to the substrate, has to be different to obtain net etching rates, rather than net deposition of a thin coating. For Cr and Ti bias voltages of more than -750 V and -380 V are needed, respectively [26].

2.4 Adhesion of Thin Films

The term adhesion is defined as the mechanical strength of the joint between two different materials or objects. Applied to coatings, adhesion is the work necessary to detach the coating from the substrate, therefore an indicator for the adherence of a film. The adhesion properties are fundamental for the overall performance of the thin film. The bonding occurs on the atomic (chemical bonding) or the macroscopic level (mechanical bonding). These chemical bonding can be ionic, covalent, metallic, or a mixture of these. Furthermore, Van der Waals forces or dispersion boning are referred to as chemical bonding types. Adhesion through mechanical bonding is interlocking (“keying”) of two surfaces, typically present on rougher surfaces. The bonding strength is higher for chemical bonding an should be preferred [28].

The measurement of adhesion is usually happening through a mechanical test, either applying forces normal to the film surface (e.g. direct pull-off method, HRC-adhesion test) or lateral (e.g. scotch tape method, peel test, scratch-test). The gained values for the adhesion are not directly comparable to each other. A distinction must be made between the possible maximum adhesion, the basic adhesion (*BA*), and the experimentally measured adhesion (*EA*). A basic relationship of *BA* and *EA* is given through Equation (2.1), involving the internal stresses (*IS*) and the method-specific error (*MSM*) of the used measurement [29].

$$EA = BA - IS \pm MSM \tag{2.1}$$

There are many different properties influencing the adhesion properties of the coating. Coating dependent properties involve the residual (internal) stresses of the coating and the film morphology. Residual stresses evolve from the difference in the thermal coefficient and lattice mismatch of the coating and substrate. Furthermore, the presence of contaminants, incorporation of gases and lattice defects reduce the adhesion. To reduce the stresses in the coating and to enhance the chemical bonding forces between the thin film and substrate, the interface region has to be optimized. Typically, the interface regions are categorized in [7]:

- Abrupt interfaces
- Mechanical (interlocking) interfaces
- Diffusion (or graded) interfaces
- Compound interfaces (also requires diffusion)
- Pseudo-diffusion interfaces (physical mixing, implantation)
- Combination of these

Figure 2-6 illustrates these different interface regions. Abrupt interfaces are present, when there is no or low diffusion and is characterized through sudden changes in material properties within the distance of atomic spacing. Mechanical interlocking interfaces are abrupt interfaces on rough substrates and can either enhance the adhesion or weaken it, depending on the ability of the deposited film "fill in" the rough spots. In diffusion interfaces a gradual change from coating to substrate is observed. Generally, diffusion leads to good adhesion but if the diffusion layer

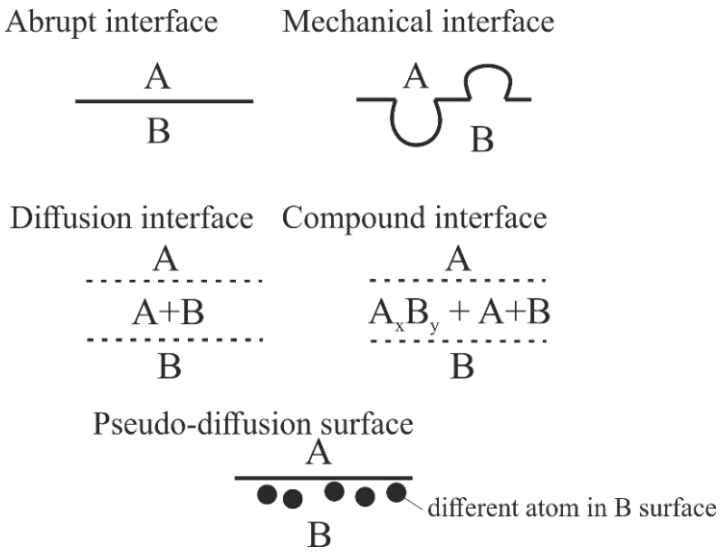

Figure 2-6: Interface regions.

is to thick pores could occur, weakening the adhesion. Compound interfaces form, if diffusion along with chemical reactions appear. Mostly, the compounds are often brittle and introduce stresses in the coating, weakening the bonds. Pseudo-diffusion interfaces can be formed through recoil implantation during the bombardment with ions. Also, it is called pseudo-diffusion if a graded interface is formed during deposition (e.g. deposition of pure Cr before CrN). The present interface region highly impacts the adhesion properties of the film onto the substrate and therefore the modification and optimization are of high importance. The alteration of the interface can be done prior to the coating process (e.g. pseudo-diffusion interface using metal ion etching), during (e.g. activation of diffusion processes through substrate heating) or after the deposition process. [7,30].

3 Structural, Morphological and Chemical Analysis

3.1 Scanning Electron Microscopy (SEM)

In material science, scanning electron microscopy (SEM) has become one of the most used imaging techniques. In the field of thin film characterization, it is commonly used for the measurement of the layer thickness, the determination of the morphology and structure of a sample.

In scanning electron microscopy, a highly focused electron beam is used to scan the surface of a specimen in a raster pattern. The beam interacts with the sample, whereby the incoming electrons will be randomly scattered. This interaction results in the reflection or the elastic scattering of electrons, so-called backscattered electrons (BSE), or in inelastic scattering of secondary electrons (SE), the emission of Auger electrons (AE) and characteristic electromagnetic radiations. All these ejected/emitted species can be detected separately and used for the characterization of the sample, i.e. imaging and chemical analysis, see chapter 3.3. These interactions all take place in a pear-shaped volume in the specimen, see Figure 3-1. The depth of this volume ranges between several nanometres up to several micrometres, depending on the energy of the impacting electrons, the density and atomic number *Z* of the sample. The ejection of secondary electrons occurs in surface near areas, therefore the collection of these, typically using an Everhart-Thornley detector, is used for topographical imaging. Backscattered electrons allow for imaging with respect to the atomic number, areas with higher atomic number appear brighter on the corresponding image [31,32].

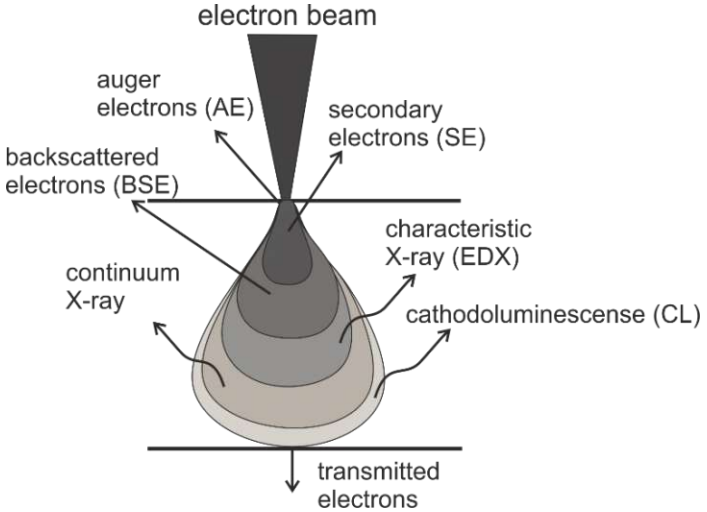

Figure 3-1: Pear-shaped interaction volume of electron beam and sample.

3.2 Transmission Electron Microscopy (TEM)

Transmission electron microscopy has been proven to be a powerful and versatile analytical method in the field of material science. It is possible, required that the TEM is equipped with the necessary detectors, to obtain an insight about the elemental composition, morphology, the crystal structure, the oxidation states of the elements, bond distances and the nature of bonding of these elements. High resolution images can be obtained and distances of around 0.5 Å are clearly distinguishable nowadays. The big downside is, that the preparation of the samples is tricky and time-consuming. For metals, typically the maximum thickness of the specimen must not exceed 100-150 nm [33].

The signal generation in TEM takes place, as with SEM, through a focused electron beam, which interacts with the matter of the specimen and produces a variety of signals, see Figure 3-1. The transmitted electrons, either without interaction or inelastically/elastically scattered, are then used for most detection methods. The relativistic de Broglie equation, Equation (3.1), shows that the wavelength of the electrons λ depends on their velocity v, which can be altered through the acceleration voltage V in the electron gun of the microscope. Other influencing factors are the Planck's constant h, the rest mass of the electron m_0, the charge e of an electron and the speed of light c. In commonly used devices, the acceleration voltage ranges between 100 and 300 kV, with corresponding wavelengths of 3.7 pm and 2 pm, respectively. These wavelengths lead to the high magnification values reached in TEM [34].

$$\lambda = \frac{h}{m_0 v\sqrt{1-\frac{v^2}{c^2}}} = \frac{h}{\sqrt{2m_0 eV\left(1+\frac{eV}{2m_0 c^2}\right)}} \tag{3.1}$$

Basically, there are two TEM techniques that are distinguished, conventional TEM (CTEM) and analytical TEM. Commercially available TEMs often utilize tools of CTEM and analytical TEM [35]. A short overview of the TEM techniques, used within this thesis, is given below. An insight of EDS is given in section 3.3.

High Resolution Transmission Electron Microscopy (HRTEM)

HRTEM is considered a CTEM method and is based on phase contrast for imaging. The electron wave interferes with the sample, undergoes a phase change and is recorded as a so-called image wave by a CCD - detector (charged-coupled device). Images can then be processed using contrast transfer functions. This method is capable of reaching resolutions of 0.5 - 0.8 Å, which allows to investigate the crystalline structure, down to individual atoms and defects [35].

Selected Area Electron Diffraction (SAED)

SAED is a crystallographic experimental technique used in TEM, similar to X-ray diffraction, except that electrons are used to obtain a diffraction pattern. Due to the small wavelength of the electrons, see Equation (3.1), they are scattered by the atoms of a solid in particular angles while others pass through without interaction, resulting in an crystal specific pattern. The area, which the diffraction pattern is obtained, can be easily selected by the user with an selected area aperture [36].

Scanning Transmission Electron Microscopy (STEM)

In STEM the focused electron beam scans the specimen in a grid like pattern and collecting the generated signals for each pixel. In this mode microanalytical (EELS, EDS) and imaging (DF, BF, HAADF) signals can be collected at the same time. The mostly used imaging mode is HAADF (high-angle annular dark field), where high angular, incoherently scattered electrons are collected for imaging. Elements with higher Z (atomic number) scatter more electrons at higher angles [37].

Electron Energy Loss Spectroscopy (EELS)

In TEM high energy electrons, with a narrow energy distribution, pass through a thin sample and inelastic/elastic scattering takes place. The electrons loose energy depending on the chemical composition, the electronic structure of the material, the chemical bonding of the elements and the nearest neighbour distances. The transmitted electrons are then detected in a specific angular range through an electron spectrometer in an EELS detector. The generated signal provides information on all the previous mentioned properties, but the interpretation can be difficult [38].

3.3 Energy Dispersive X-Ray Spectroscopy (EDX, EDS)

Energy dispersive X-ray spectroscopy (EDX or EDS) is widely used to obtain an insight about the chemical composition of a specimen, because the creation of X-rays is a typical by-product of other analytical methods. Within this thesis the generation of X-rays will be limited to the bombardment with a focused electron beam, which is used in SEM and TEM.

During SEM or TEM analysis a highly focused electron beam hits the surface, interacts with the specimen and ejects an electron of the inner atom shell, typically from the K- or L-shell. The remaining vacancy is then filled with an electron from an outer shell resulting in a release

of an element characteristic energy, either in the form of X-ray photons or Auger electrons. These characteristic X-rays are detected and give information about the chemical composition, as well as the weight and atomic percent of the containing elements. The detection accuracy reaches down to 0.1 wt.% or even lower, depending on the atomic number of the element, whereas the atomic number should exceed the one of boron (Z = 4) to be sufficiently detectable [32,39].

3.4 X-Ray Diffraction (XRD)

X-ray diffraction is a widely used method for the characterization of solid materials. Through this technique the crystalline structure, grain sizes, textures, residual stresses and information on the crystalline phases can be determined.

$$n\lambda = 2d \sin\theta \tag{3.2}$$

The principle of XRD is based on Bragg's Law, Equation (3.2), which describes the phenomenon of diffraction of waves on periodic structures, such as crystalline solids. This equation is fulfilled, equal to constructive interference, when the diffraction order n and the wavelength λ are in relation with the interatomic distance d and the incident angle θ of the electromagnetic wave. Figure 3-2 illustrates Bragg's Law. X-rays are used, due to the fact that their wavelength is in the same dimension as the distance between the crystal lattice planes. Most XRD patterns are recorded using Cu-K_α radiation, with a wavelength λ of 1.542 Å. The present phases are usually identified by comparing the position of the Bragg peaks of the XRD pattern of the tested sample with reference patterns from databases, like the PDF- (Powder Diffraction File) database from the International Center for Diffraction Data [40].

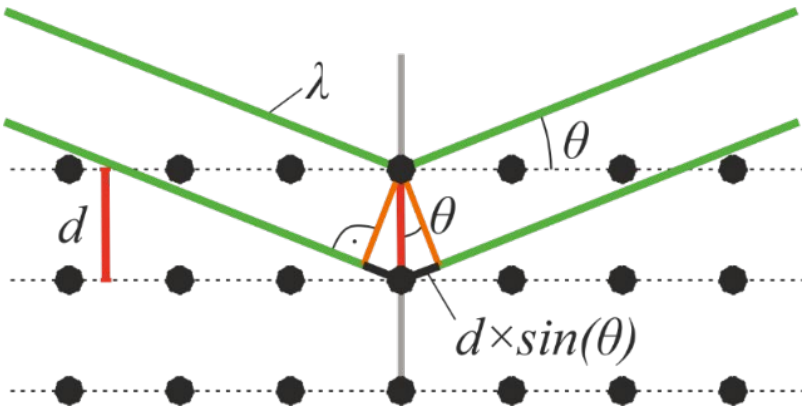

Figure 3-2: Schematics of the diffraction of electromagnetic waves on atomic lattice planes – Bragg's Law.

3.5 Secondary Ion Mass Spectroscopy (SIMS)

In the application of surface analytics SIMS is one of the most used methods. The result is a spectrum of the chemical composition of a specimen, with a very high sensitivity of around 1 ppm for all elements.

In secondary mass spectroscopy an ion beam bombards the surface of the specimen with positive ions (e.g. Ar^+, $SF5^+$, Ga^+). The incident ion causes a collision sequence in the surface near region of the specimen, leading to the ejection of positive and negative secondary ions and neutral atoms or particles and electrons (sputtering), see Figure 3-3. The secondary ions are then detected by a mass analyser, although more than 90% of ejected species are neutral particles. The most used detectors are either quadrupole mass spectrometers, time-of-flight mass spectrometers or magnetic sector field. SIMS requires even ultra-high vacuum (UHV) conditions (pressure below 10^{-6} mbar) [41].

Based on the energy density of the ion beam, and the resulting impact on the surface of the specimen, SIMS can be distinguished into static or dynamic SIMS. Static SIMS is a surface sensitive method, whereas dynamic SIMS is used for bulk analysis, with ion doses higher than 10^{11} ions/mm^2. Further, it is possible to measure a depth profile or a three-dimensional element distribution [42].

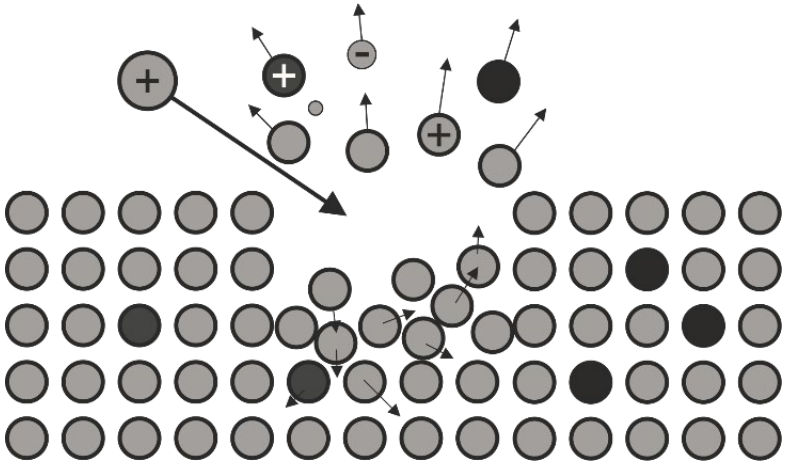

Figure 3-3: Schematic collision cascade of SIMS.

3.6 Elastic Recoil Detection Analysis (ERDA)

Elastic recoil detection analysis utilizes an ion beam (generated by an ion accelerator) to give a depth profile of the element concentration, mostly of thin films. The atoms of the investigated sample (target) are recoiled in forward direction by the high energetic incident ions (e.g., I^{8+}, Br^{8+}). The projectiles hit the target with an incidence angle α. The recoiled target ions, which leave the surface with an exit angle β, are detected at the recoil angle θ, see Figure 3-4. To achieve this recoil, the mass M_1 of the impacting ions has to be higher than the mass M_2 of the target atoms. Therefore, theoretically, all elements can be detected using ERDA, resulting in a broad energy range (from around 2-100 MeV) for the projectiles. The depth information is obtained from the energy difference of the recoiled atoms – ions from a specific depth have a lower energy than those from the surface. Depending on the energy of the recoiled ions, different detectors are common. For low energies (approx. 2-10 MeV) silicon diode, for medium energies (approx. 30 MeV) time-of-flight and for high energies (up to 100 MeV) gas ionization detectors are used [43].

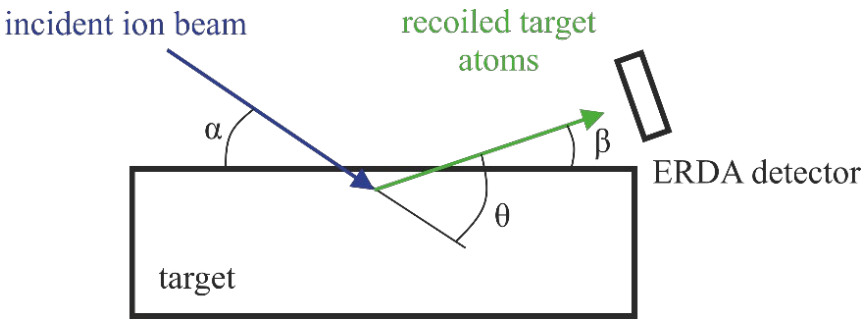

Figure 3-4: Schematic geometry of ERDA.

3.7 Rutherford Backscattering Spectrometry (RBS)

Rutherford backscattering spectrometry (RBS) is a non-destructive nuclear method used for determining the elemental composition of thin films in the nanometre and up to the micrometre scale. An ion beam (mostly protons or He^+) impinges the surface of a sample, leading to the backscattering of the used ions, see Figure 3-5. The interaction is described as an elastic, hard-sphere collision between the impinging ion and the bound atom of the sample (also referred to as target). The initial energy E_0 of the projectile ion with the mass M_0, changes due to the collision. The resulting energy E_S after the backscattering event depends on the mass of the incidenting ion M_0, the mass of the substrate atom M_i (or the atomic number Z, respectively), the depth x at which the ion gets scattered, the scattering angle θ and the initial energy of the projectile ion E_0. This means, that the loss of energy mainly depends on the mass and the depth

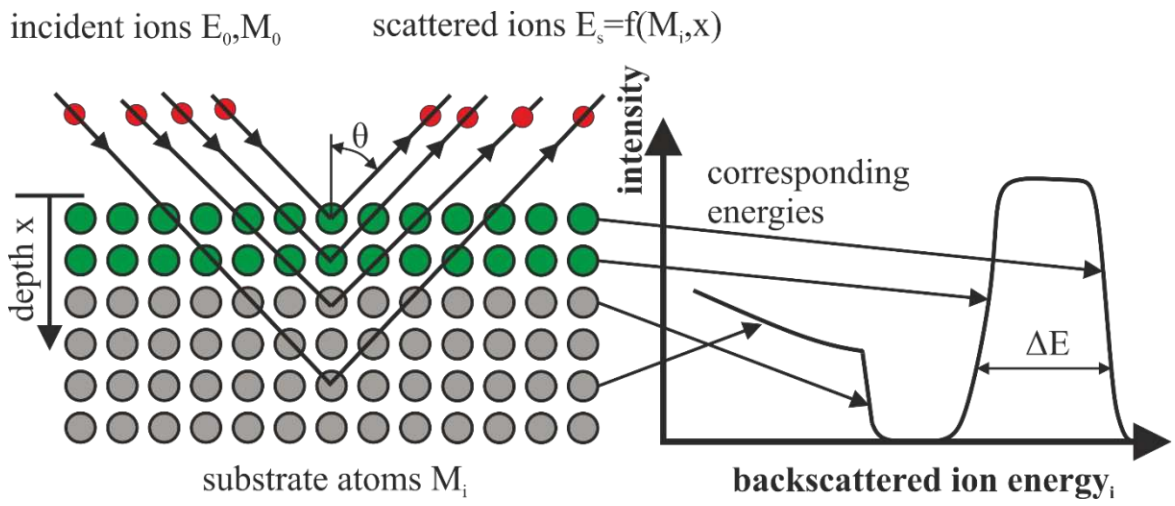

Figure 3-5: Schematic illustration of ion interaction of RBS with corresponding graph of the intensity over the energy of the backscattered ions.

of the target atom, at which the scattering event occurs. Therefore, a depth profile of the chemical composition of the sample can be obtained. In Figure 3-5, the corresponding energies, depending on the depth, are illustrated. The obtained RBS spectrum is the intensity of the scattered ions (or yield of these) versus the channel, which corresponds to the energy of the backscattered ions. The best sensitivity of RBS is obtained, if the chemical composition of the sample is already known beforehand [41].

4 Mechanical Analysis

In this section an overview about the mechanical analysis techniques used during this thesis is given. These methods characterize the mechanical properties of the samples, especially the hardness and the adhesion properties of coatings.

4.1 Optical Profilometry

During this thesis optical profilometry was mainly used to study the residual stresses in the coating on silicon substrates, due to the curvature of the samples. Furthermore, it was used to determine the surface roughness of the coatings and substrates.

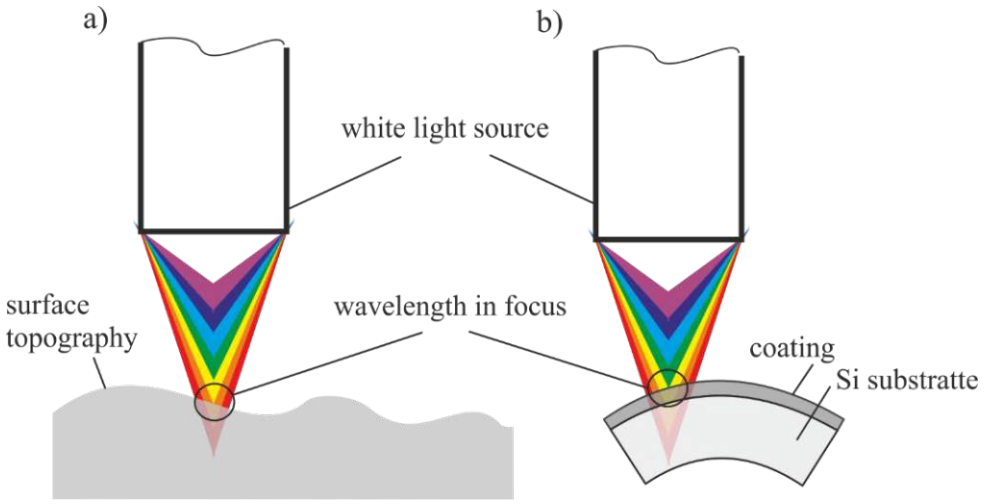

Figure 4-1: Schematic profilometry measurement of a) surface topography, b) curvature of substrate (compressive stresses).

The used profilometer uses a white light source (LED), with a high degree in chromatic aberration. Due to an array of lenses, each wavelength of the white light is in focus at a different distance to the specimen, resulting in the vertical measurement range. The wavelength, which reflects sharply while all the others are out of focus, passes through a filter and reaches the charged-coupled device (CCD) detector, see Figure 4-1. This means, that a direct information about the topography of the sample is given and no further algorithm is needed. The surface roughness and topographical images can then be processes using the gained data [44].

$$\sigma = \frac{E}{(1-\nu)}\frac{D^2}{6Rd} \tag{4.1}$$

$$R = \frac{L^2}{8\delta} \tag{4.2}$$

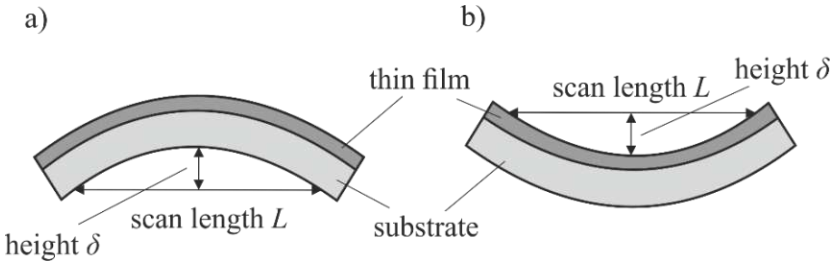

Figure 4-2: Bending of the specimen due to a) compressive stresses, b) tensile stresses.

The residual stresses σ in the coating can be calculated through the curvature R, Young's modulus E, Poission's ratio v, and the thickness D of the substrate and the coating thickness d, utilizing the simplified Stoney-equation, Equation (4.1). Furthermore, the curvature R is determined through the length of the scan L and the height δ, Equation (4.2). These values are readings of the optical profilometer. Figure 4-2 shows the bending of the sample due to the residual stresses in the coating. Residual stress values lower than zero are equal to compressive stresses, otherwise tensile stresses are present [45].

4.2 Nanoindentation

The hardness of a material is defined as the resistance against the penetration of another body and the accompanying plastic deformation. Various experiments are used to define this characteristic property, all with different testing conditions. Therefore, the hardness values of different testing methods are not directly related to each other. The most common hardness measurement methods are Brinell (HB), Vickers (HV), and Rockwell (HR), each using different indenter shapes, parameters and calculation models. Common for all tests is that a predefined load is applied, which forces the indenter into the tested sample [46,47].

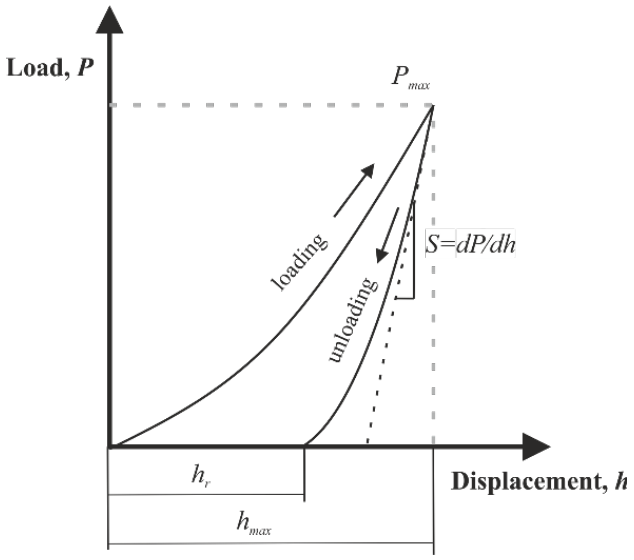

Figure 4-3:Typical load/displacement curve during nanoindentation [50].

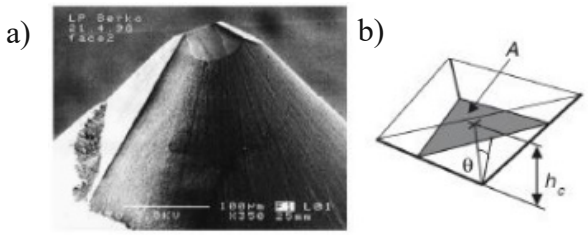

Figure 4-4: Berkovich indenter a) SEM image of the indenter, b) indenter geometry [48].

Since the coating thickness of thin films is in the range of a few micrometres, the penetration depth of conventional hardness testing techniques is too deep, therefore nanoindentation is used for the hardness determination. The indenter penetrates the surface of the specimen, using a certain load, and followed by an unload sequence. During this load/unloading cycle, a load displacement curve is recorded, Figure 4-3. The most used indenter shape is a Berkovich diamond tip with a face angle θ of 65.27°, see Figure 4-4. The projected area A, measured from the depth of the circle of contact h_c, is nearly the same as for Vickers indenters [48]. The hardness and the indentation modulus can be calculated by the method of Oliver and Pharr [49]. The hardness is the ratio of the maximum load P_{max} and the remaining contact area A, which can be determined through the shape of the indenter and the penetration depth h. The indentation modulus can be determined through the slope S of the unloading curve [50].

4.3 Tribometer – Oscillating Wear Test (SRV)

For the qualitative examination of the adhesion behaviour of the coating onto the substrate, a tribometer was used. This experimental setup allows a fast and easy characterization of adhesion properties, but only a direct comparison between related tribological systems is valid.

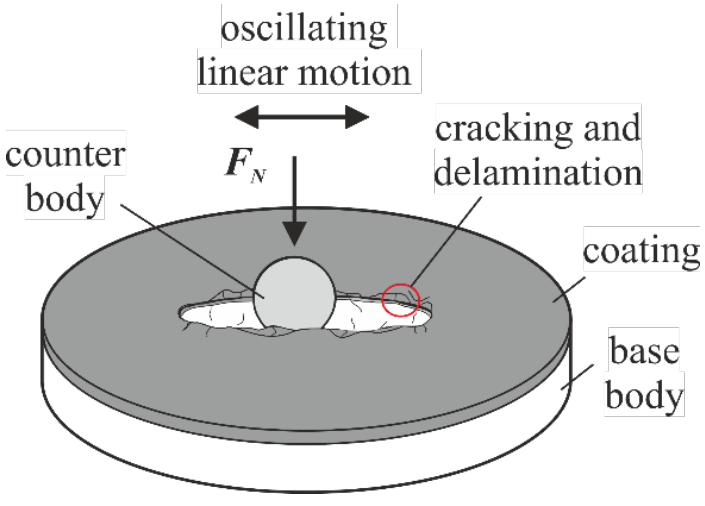

Figure 4-5: Schematically illustration of a SRV-test.

Tribology is the study of mutually interacting surfaces in relative motion and acts as a collective term, covering the fields of friction, wear and lubrication. A tribometer provides information about the behaviour of a tribological system, which contains of the base and counter body, an intermediate medium and the environment [51].

For the oscillating wear tests the counter body, e.g. a ball, is loaded with a normal load F_N and slides in a linear, oscillating motion with a velocity v across the base body. Figure 4-5 illustrates an SRV-test of a coated base body. Indications for poor adhesion of the coating are spalling, cracking and delamination of the coating on the edge of the wear track.

4.4 Rockwell (HRC-) Adhesion Test

The Rockwell (HRC-) adhesion test, often referred to as Daimler-Benz adhesion test, is a fast and easy characterization method to properly identify the adhesion properties of thin films.

The Daimler-Benz adhesion test was first described by the VDI guideline 3198 [52]. A Rockwell diamond cone is forced into the surface of a coated substrate with a defined force, typically 1471.5 N. For softer materials lower forces are valid. The resulting imprints are then investigated using an optical microscope or SEM. On the boundary of the indentation, spalling, cracking and delamination can occur, which are indications for poor adhesion properties of the coating. Due to the degree of this failure indicators, the imprints are classified in failure categories (HF1-HF6), according to the VDI guideline 3198, see Figure 4-6 [52]. This guideline has since been rejected and is replaced by the international norm DIN EN ISO 26443 [53],

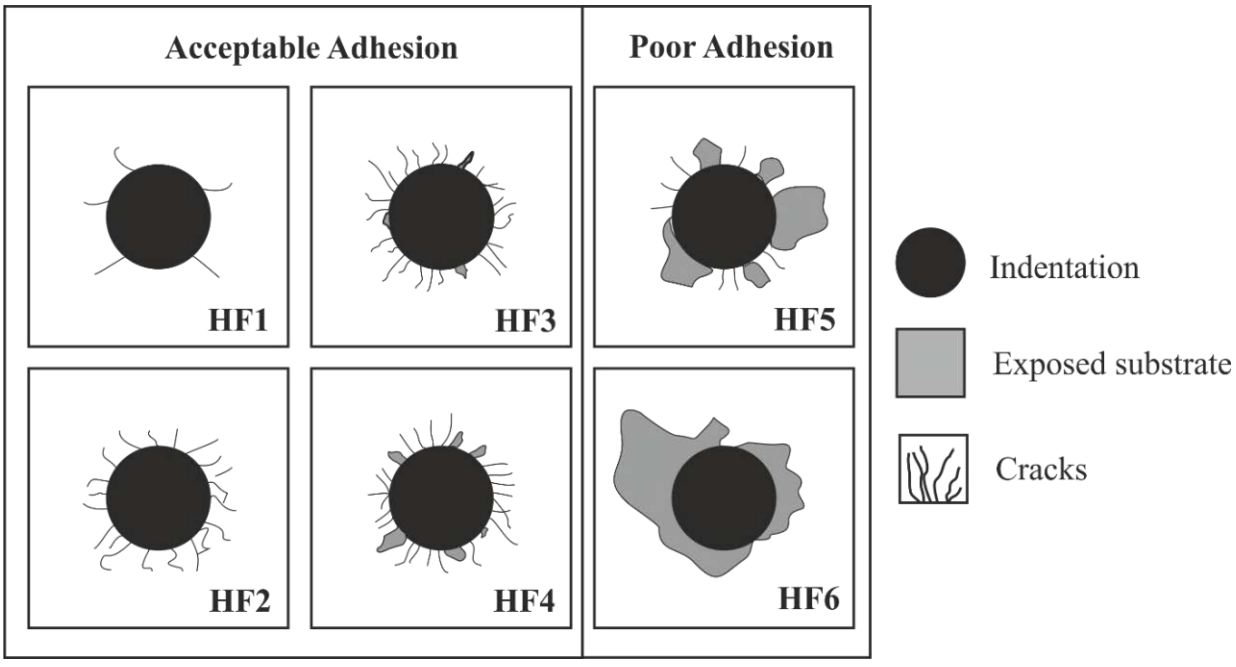

Figure 4-6: Classification categories HF1-HF6 after VDI 3198 [52].

which only defines 4 failure categories, but are based on the VDI guideline. Commonly, the categories after VDI 3198 are used in publications.

Due to experience, the categories HF1-HF4 show acceptable adhesion properties for most applications. Only the formation of cracks and small areas of spalling are present on the edge of the imprint. On the other hand, HF5 and HF6 expose a high degree of spalling on the boundary of the indentation and therefore subpar adhesion properties. At the HF6 failure category delamination of coating is present over the whole border region of the imprint.

5 Experimental Setup

In a fuel injection pump, the injection valves regulate the flow of the fuel to the injection chamber. If the valve ball opens, fuel can pass through, otherwise the valve ball presses onto the valve seat, closing the fuel path. The combination of the high number of open/closing cycles throughout the lifespan of the valve with the resulting high surface pressures on the valve seat and poor-quality fuels, results into high requirements on the used materials. To fulfil the demand, the valve seat is coated, mostly using CrN, see Figure 5-1, resulting in advanced performances. However, for better and sufficient combustion, injection pressures of more than 2000 bar are used, causing delamination of the coating in the valve seat. To obtain better adhesion properties of the coating, the experimental setups described in this chapter were conducted.

The following section is divided into three different experimental setups. The first experimental setup focuses on the optimization of the CrN coating. A few requirements had to be fulfilled, to mimic the properties of the industrially used coating for this application. The obtained CrN coating acts as a baseline for the following tests.
As a second step, different testing series were conducted, regarding the influence of the etching processes on the adhesion properties of the coating onto the two different alloyed and surface pre-treated steel substrates (later referred to as nitrided or hardened steel). To obtain results, mimicking the real application as closely as possible, the etching and deposition procedures were conducted on actual valve pieces (as they are used in injection pumps), as illustrated in Figure 5-1. Additionally, Si and austenite substrates were placed into the substrate holder along with the valve pieces.

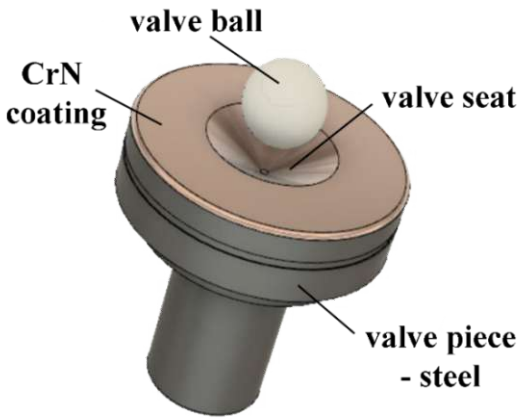

Figure 5-1: Illustration of a coated valve piece.

Figure 5-2: “Noreia” deposition plant [54].

A further testing series had been performed, to obtain an insight in the implantation depth of Cr-ions in the substrate surface. Therefore, only Cr-ion etching processes were conducted and the substrates were coated with a Mo-layer. All coating and etching processes were conducted using the “Noreia” deposition plant, Figure 5-2. It is equipped with two 5kW HiPIMS and two DC generators, which can either power the cathodes or are used for the bias potential of the substrate. Furthermore, the system is capable of heating the substrate up to 800°C. The configuration used, consists of two 6-inch (Cr-Target) cathodes and one 3-inch (Mo-target) cathode [54].

5.1 Coating Optimization

The goal of this testing series was to mimic the properties of a well-established CrN coating to obtain a baseline for the further adhesion investigations. The requirements, the final coating has to fulfil, are:

- Coating thickness around 4 µm
- Hardness of the coating roughly ≥ 20 GPa
- Internal stresses in the coating 1-3 GPa compressive stresses
- Process temperature lower than 300 °C
- Chemical composition of CrN slightly over-stoichiometric in nitrogen
- Orientation of CrN thin film (200)
- Deposition of an approximately 250-300 nm thick Cr interlayer between CrN and substrate

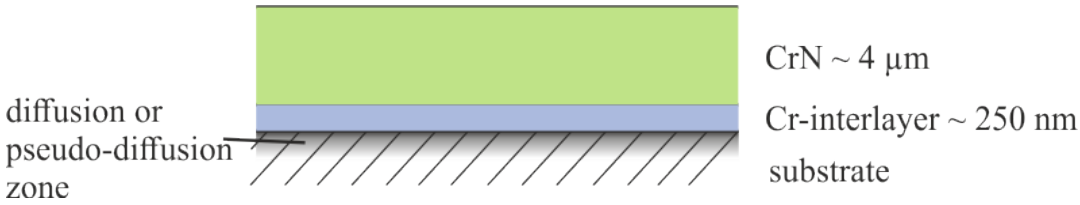

Figure 5-3: Desired coating structure.

Figure 5-3 shows the required coating structure. A Cr-interlayer is deposited prior to the CrN coating. A diffusion or pseudo-diffusion zone is indicated between interlayer and substrate. For the following testing series, the coating and interlayer were deposited on silicon (Si) and austenite substrates, due to their defined and well-known properties. The deposition parameters, which are constant for all different coating process, are as follows:

- Targets used for the interlayer and CrN coating – Cr HP 99.8% (Plansee Composite Materials GmbH)
- Argon etching for 15 min with bias potential U_{bias} = -400 V
- Current controlled process for deposition of interlayer and coating – I = 4.2 A resulting in a power density of ~ 10 W/cm^2
- Height of the z-axis – z = -150 mm (internal "Noreia" height parameter)
- Pressure during deposition of interlayer and coating – p = 4 µbar
- Time for interlayer deposition – $t_{interlayer}$ = 3 min

The different coating parameters can be seen in Table 5-1. The ratio of N_2 to Ar was based on experience, to obtain a slightly over-stochiometric coating crystallizing in single-phased cubic (B1, NaCl-prototype) structure. A bias potential (U_{bias}) variation was conducted, to introduce compressive stresses into the coating. The substrate temperature T during the coating, was chosen based on the maximum allowed temperature. To obtain the coating time, for reaching the desired 4-5 µm thick coating, a deposition process was conducted, and the deposited coating thickness was measured, resulting in a time dependet deposition rate. The parameters changed during the different coating runs are highlighted in red.

Table 5-1: Coating parameters for the coating optimization testing series

Ratio N_2:Ar []	T [°C]	U_{bias} [V]	Coating time t_{coat} [min]
75:25	200	float	25
75:25	200	-50	90
75:25	200	-100	90
75:25	300	float	25
75:25	300	-50	90
75:25	300	-100	90
80:20	200	float	95
80:20	200	-50	95
80:20	200	-100	95
80:20	300	float	95
80:20	300	-50	95
80:20	300	-100	95

5.2 1st Setup – Adhesion Improvement

Since the experiments should depict the real application as close as possible, the coating and etching procedures were conducted on valve pieces (either made of hardened or nitrided steel). Therefore, a substrate holder had to be designed and manufactured, see Figure 5-4. The valve pieces are fixated from the backside using clamps. Furthermore, inserts for standardized Si- and austenite substrates are present for easier characterization. The valve pieces are recessed, meaning the height of the surface, which is coated, of the austenite, silicon and valve pieces is the same for all substrates, eliminating a potential influencing factor (due to different distances from substrate surface to target) of the deposition process.

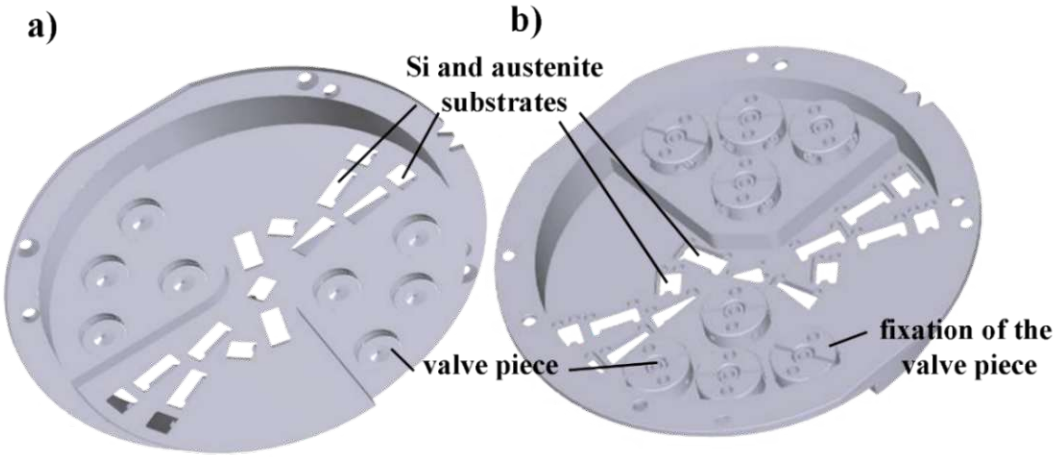

Figure 5-4: Illustration of the used substrate holder a) bottom-up view, b) top-down view.

As a first study of the influence of the etching process on the adhesion properties, four different etching procedures were compared – details can be seen in Table 5-2. For Cr-ion etching a higher U_{bias} was used, since for bias potentials lower than -700 V a net deposition can be observed (see chapter 2.3.1). Furthermore, higher U_{bias} is beneficial to the implantation of Cr-atoms into the surface [23]. After the etching process, a Cr-interlayer and CrN coating was deposited, using the parameters for the baseline coating, see chapters 5.1 and 6.1. At this testing series, the etching and coating processes were conducted at 200 and 300 °C, respectively. The z-height was z = -150mm for all tests.

Table 5-2: Parameter table adhesion improvement 1st experimental setup

Etching procedure	T [°C]	U_{bias} [V]	Etching time t_{Etch} [min]
Ar-etching	200	-400	10
	300		
N_2-etching	200		
	300		
Forming gas-etching	200		
	300		
Cr-ion etching	200	-700	
	300		

For the Ar-etching process, Argon is the working gas used during the etching process, meaning the Ar-ions bombards the substrate surface. The N_2-etching process utilizes nitrogen (N_2) gas. During forming gas-etching a mixture of a mixture of 95% Ar and 5% H_2 had been used as the working gas, with the goal to create chemical, along with physical, etching conditions. To produce the Cr-ions, a 6-inch Cr HP 99.8 % target was used in HiPIMS mode. The HiPIMS parameter setup can be seen in Table 5-3.

Table 5-3: HiPIMS parameter for Cr-ion etching

Parameter	
average power $P_{AVR.}$	1000 W
frequency f	75 Hz
on-time t_{on}	75 µs

As mentioned, the Cr-ions were created by applying a HiPIMS signal to a 6" Cr-target. Beside Cr^+ (or Cr^{2+}), also neutral Cr-atoms are ejected from the target surface, as it can be seen in Figure 5-5. As displayed, a raised shutter configuration is used, which shields the substrate from the created neutral Cr-atoms (displayed green). These neutral Cr atoms would not contribute to the etching process, in contrary, they would deposit on the substrate surface. The applied negative BIAS potential, resulting in an electric field, guides the Cr^+-ions (displayed red) on curved trajectories towards the substrate, whereas the neutral atoms are not influenced by the electric field. The ions then impinge on the surface and sputter-etch the substrate surface. Furthermore, Cr-ions are implanted into the surface, as already mentioned in chapter 2.3.1.

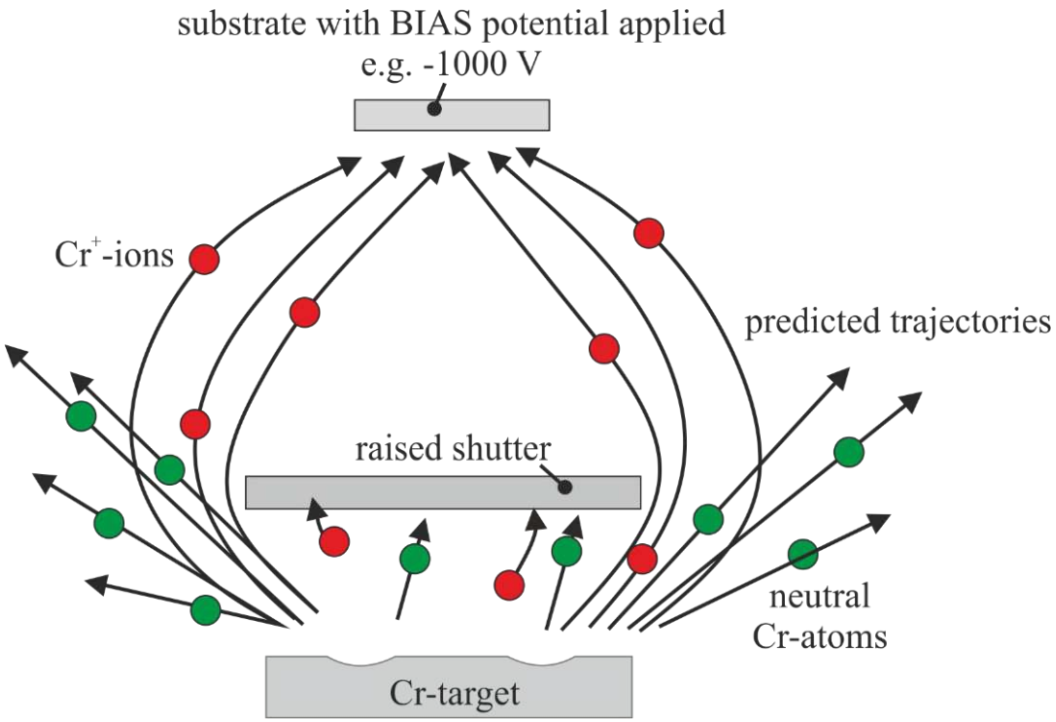

Figure 5-5: Schematic of the target-shutter-substrate configuration with the predicted trajectories for the Cr^+-ions and the neutral Cr-atoms, respectively.

5.3 2nd Setup – Adhesion Improvement

As later discussed in chapter 6.2, the adhesion properties after the first experimental setup had been subpar. One approach to improve the adhesion was to optimize the cleaning process prior to the deposition. From now on, following substrate cleaning sequence was conducted in the given order:

1. 5 min. cleaning in ultrasonic bath using a 3% "Deconex HT 1401" solution [55]
2. 5 min. cleaning in ultrasonic bath using a 3% "Deconex HT 1170" solution [56]
3. 4 times, 10 min. each, cleaning of the samples in fresh deionized water
4. 5 min. cleaning in ultrasonic bath using aceton
5. 5 min cleaning in ultrasonic bath using ethanol

To remove hydrocarbon surface contaminates "Deconex HT 1401" and "Deconex HT 1170" were used. These are alkaline cleanser, specifically design to remove residues of anti-corrosive and machining oils. The further steps were conducted to clean the samples from the alkaline solution because any residues could again weaken the adhesion properties.

Another approach to increase the adhesion of the coating is to optimize the etching process. The etching time was increased from 10 to 100 minutes. To increase the energy of the impinging ions, cleaning the surface, the bias potentials were increased up to -1000 V, which is the maximum capability of the generators. Furthermore, the etching and deposition processes were conducted only at 200 °C, since the temperature dependency is negligible. The z-height during the etching processes was constant at z =-150 mm. Table 5-4 gives an overview of the parameter set for the experimental series.

Table 5-4: Parameter table adhesion improvement 2nd experimental series

Etching precedure	U_{bias} [V]	T [°C]	Etching time t_{Etch} [min]
Ar-etching	-400	200	100
	-1000		
N_2-etching	-1000		
Forming gas-etching	-1000		
Cr-ion etching	-700		
	-1000		

5.4 3rd Setup – Adhesion Improvement and Etching Rate Determination

Since Cr-ion and forming gas etching proofed to be the most promising etching methods (please see chapters 2.3.1 and 6.2), the following testing series focused on these two etching procedures. Since the ion concentration plays a key role in the efficiency of the etching process, the following approaches to increase the ion flux and therefore the efficiency of the process, were tested, see Table 5-5. It should be mentioned that for these experiments, only the nitrided valve pieces were used as substrates.

The distance between the cathode and the substrates was reduced, the height was z = -165 mm for all the tests. Furthermore, an etching process utilizing an additional ion source (2x6" Cr-targets) was conducted. Also, in terms of the bias potential (accelerating voltage), a synchronized bias signal was used. Hereby, the HiPIMS generator powering the cathode, triggered the bias generator in order to increase the efficiency of the process of accelerating the ionized species at the exact time they are produced. Furthermore, an etching process combining Cr-ion etching and forming gas-etching was also conducted during this experimental series. The etching time is one of the most important influencing factors of the adhesion improvement, therefore long-time etching tests were conducted.

Table 5-5: Parameter table adhesion improvement 3rd experimental setup

Etching precedure	Etching time t_{Etch} [min]	T [°C]	U_{bias} [V]
Cr-ion etching, 2 sources	120	200	-1000 V
Cr-ion etching, synchronized bias	120		
	360		
Cr-ion etching, DC-bias	120		
Cr-ion etching using forming gas	120		
Forming gas etching	360		

To determine the etching rates silicon and austenite samples, partly masked with TiO_2, were used. The substrates were placed in the substrate holder, along with the valve pieces. The TiO_2 layer protects the substrate from the influence of the etching and deposition process and can be easily removed afterwards. Figure 5-6 illustrates the application of the protective layer and the impact on the substrate of the etching and deposition process.

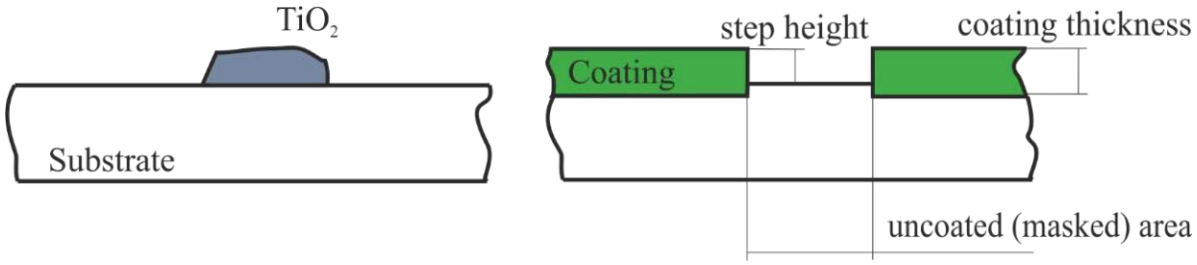

Figure 5-6: Schematic illustration of the substrates for the etching rate determination.

5.5 Implantation Depth of Cr

One of the main aspects for using Cr-ion etching is the implantation of chromium ions into the substrate material, creating a pseudo-diffusion zone. To understand the etching process and the impact in the adhesion properties, it is necessary to determine the implantation depth of the ions. Therefore, this testing series of Cr-ion etching was conducted utilizing 2 ion sources and synchronized bias, respectively. To verify the influence of the energy of the impinging ions, a variation of the bias potential was executed, see Table 5-6. The tests were conducted using silicon and austenite samples. After the etching process, the samples were coated with a thin (around 100-125 nm) Mo-layer, to protect the top layer.

Table 5-6: Parameter table determination of the implantation depth of Cr

Etching precedure	U_{bias} [V]	T [°C]	Etching time t_{Etch} [min]
Cr-ion etching, 2 sources	-300	200	120
	-700		
	-1000		
Cr-ion etching, synchronized bias	-300		
	-700		
	-1000		

6 Results

6.1 Coating Properties

For the establishment of a baseline the CrN coating has to fulfil certain morphological, chemical and mechanical properties. To characterize the growth and chemistry of the thin film XRD and SEM investigations were conducted. The mechanical properties hardness and residual stresses were examined, by using nanoindentation and optical profilometry, respectively. For all investigations, coatings deposited on silicon substrates were used.

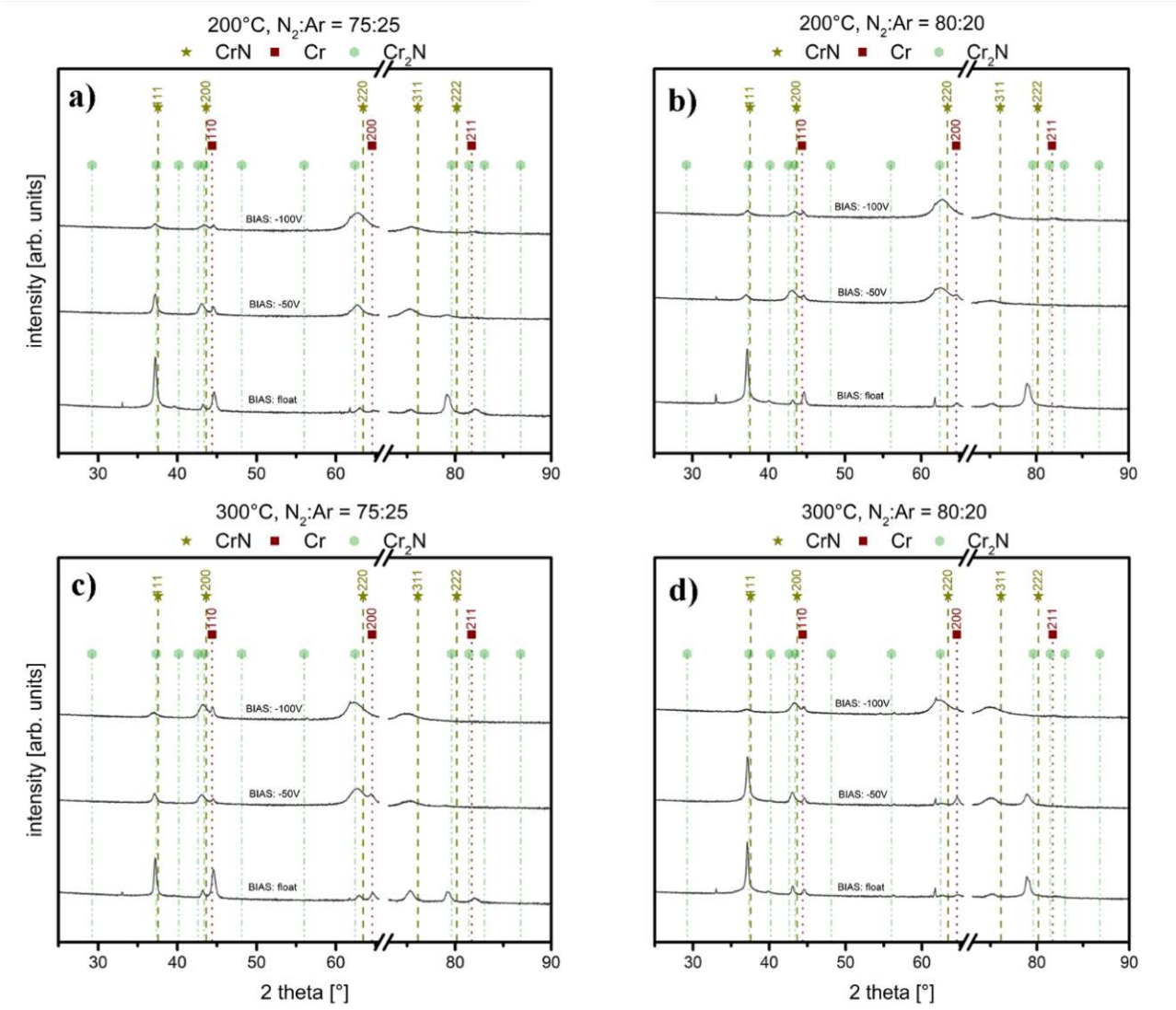

Figure 6-1: XRD-measurements in Bragg-Brentano configuration of CrN coatings at 200 °C with N_2:Ar ration of a) 75:25, b) 80:20 and at 300 °C with N_2:Ar ratio of c) 75:25, d) 80:20. The standardized peak positions for c-CrN, h-Cr and h-Cr_2N are indicated by yellow star, red cubic, and green hexagonal symbols, respectively. Furthermore, the measurements for coatings deposited using a substrate bias of floating potential, -50 V, and -100 V are displayed in a)-d) from bottom to top.

Figure 6-1 shows the XRD-measurements of the CrN coatings deposited at 200 °C and 300 °C, with gas ratios during the deposition process of 75% N_2 and 25% Ar and 80% N_2 and 20% Ar, respectively. Every graph in Figure 6-1 displays the intensity of the diffracted X-ray over the diffraction angle 2 theta, at different applied BIAS potentials.

When comparing the results in terms of the varying heater temperature and the two different gas ratios, it can clearly be seen, that these parameters show only a very minor impact on the resulting structure. On the contrary, the applied BIAS potential strongly effects the phase formation of all deposited thin films. At floating potential (meaning no external applied accelerating voltage) the XRD measurements reveal multi-phased phase composition, regardless the temperature and the applied gas ratio during the deposition. To be more specific, a mixture of h-Cr_2N and c-CrN can be identified. Here it should be mentioned that all deposited thin films reveal a h-Cr phase which can be attributed to the pure metallic Cr-interlayer. By increasing the BIAS voltage, the results reveal a clear change in the preferred orientation (from 111 to 200). Moreover, the peak observed at ~ 43° clearly shifts to higher diffraction angles (and therefore to the standardized peak position of c-CrN) pointing towards the suppression of the h-Cr_2N-phase and enhancing the formation of single-phased c-CrN with increasing BIAS potential. However, with increasing BIAS potential the resulting peaks of all measurements clearly widen up pointing towards a finer grain morphology of the coatings.

In terms of the chemical composition (obtained by EDS) of the coatings, deposited at a gas ratio of 80% nitrogen to 20% Argon, the chemical compositions are slightly over-stochiometric. EDS investigations of the resulting thin films show a composition of the CrN layer of 51-53 at-% N and 47-49 at-% Cr. Therefore, coatings deposited at an 80% N_2 to 20% Ar ration are in good agreement with industrially used coatings.

The morphology and thickness of the thin films were investigated using SEM. Figure 6-2 a) – f) shows the fracture cross-sectional micrographs of CrN coatings deposited at a 80% N_2 to 20% Ar gas ratio and varying BIAS potentials (floating, -50V, -100 V). The processes were run at 200 °C and 300 °C heater temperature, respectively. All other process parameter, e.g. power density of the target and pressure during coating, had been constant throughout the testing series, see chapter 5.1.

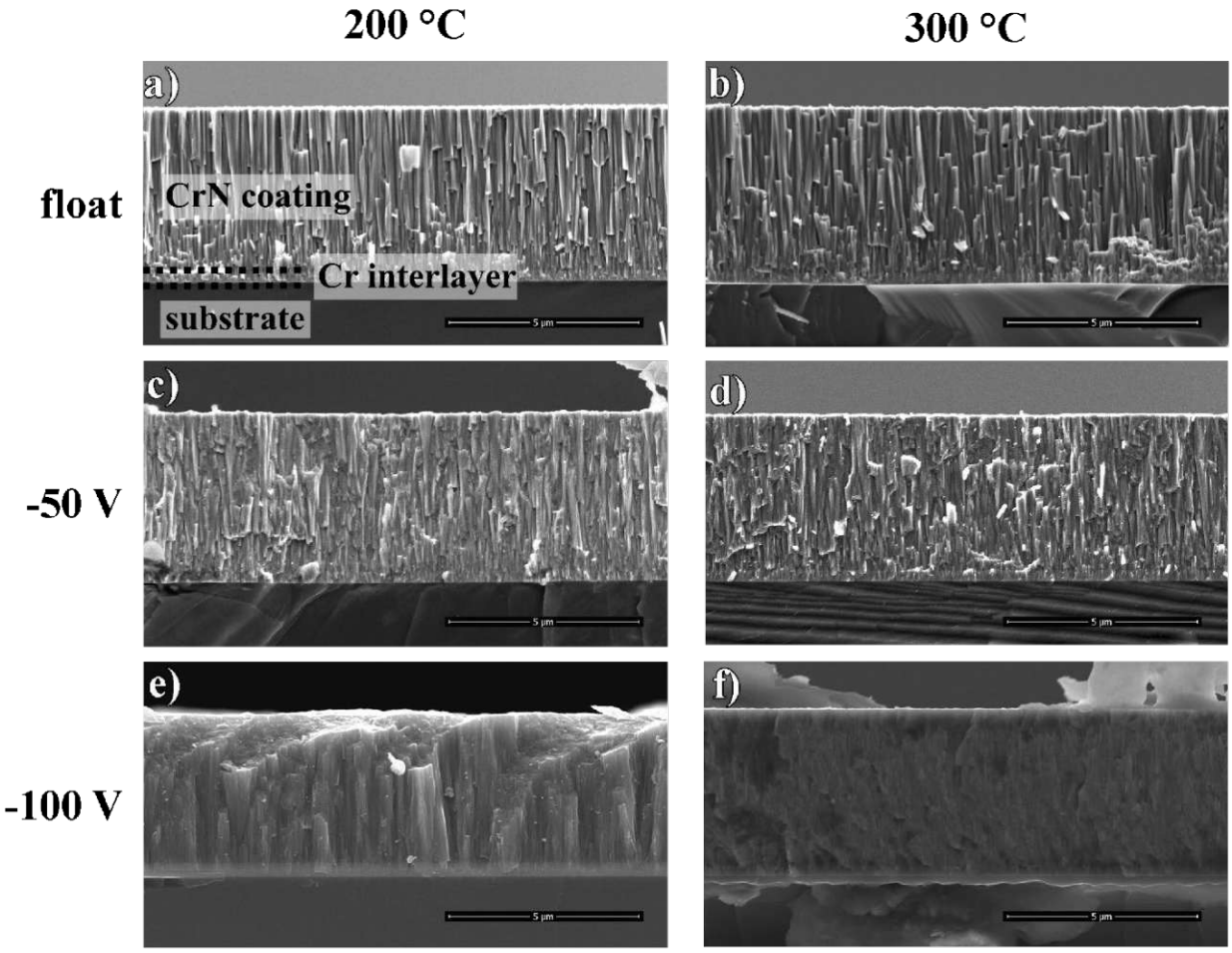

Figure 6-2: Cross-sectional images of CrN coatings deposited at 200 °C and 300°C, N_2:Ar ration of 80:20 and different BIAS potentials a) b) floating BIAS, c) d) -50 V BIAS, e) f) -100 V BIAS.

All deposited coatings exhibit a dense, columnar structure, with smaller columns for higher BIAS voltages, especially at -100 V (Figure 6-2 e), f)). This is in good agreement with the results of the XRD-measurements. Furthermore, a 270-300 nm thick Cr interlayer can be observed between the CrN thin film and the substrate. This interlayer is applied to enhance the adhesion properties of the CrN layer on the substrate and is typically done for industrial CrN coatings. The overall coating thicknesses are in the range of 4.44 µm up to 5.03 µm for the coatings deposited at 200 °C, -50 V, N_2:Ar=80:20 and 200 °C, -50 V, N_2:Ar=75:25, respectively. These coating thicknesses, along with the coating, results in deposition rates of around 44 nm/min and up to 55 nm/min, depending on the applied BIAS potential and gas ratio. Higher BIAS potentials typically exhibit lower deposition rates, than floating potentials, due to the higher energy impact, resulting in a denser morphology of the thin film. Furthermore, the coatings deposited at a gas ratio of 75% N_2 and 25% Ar are thicker than for a ratio of 80% to 20%, for the same deposition times, and therefore show higher deposition rates. This points towards a higher quantity of hexagonal Cr_2N, which is more voluminous than the cubic CrN.

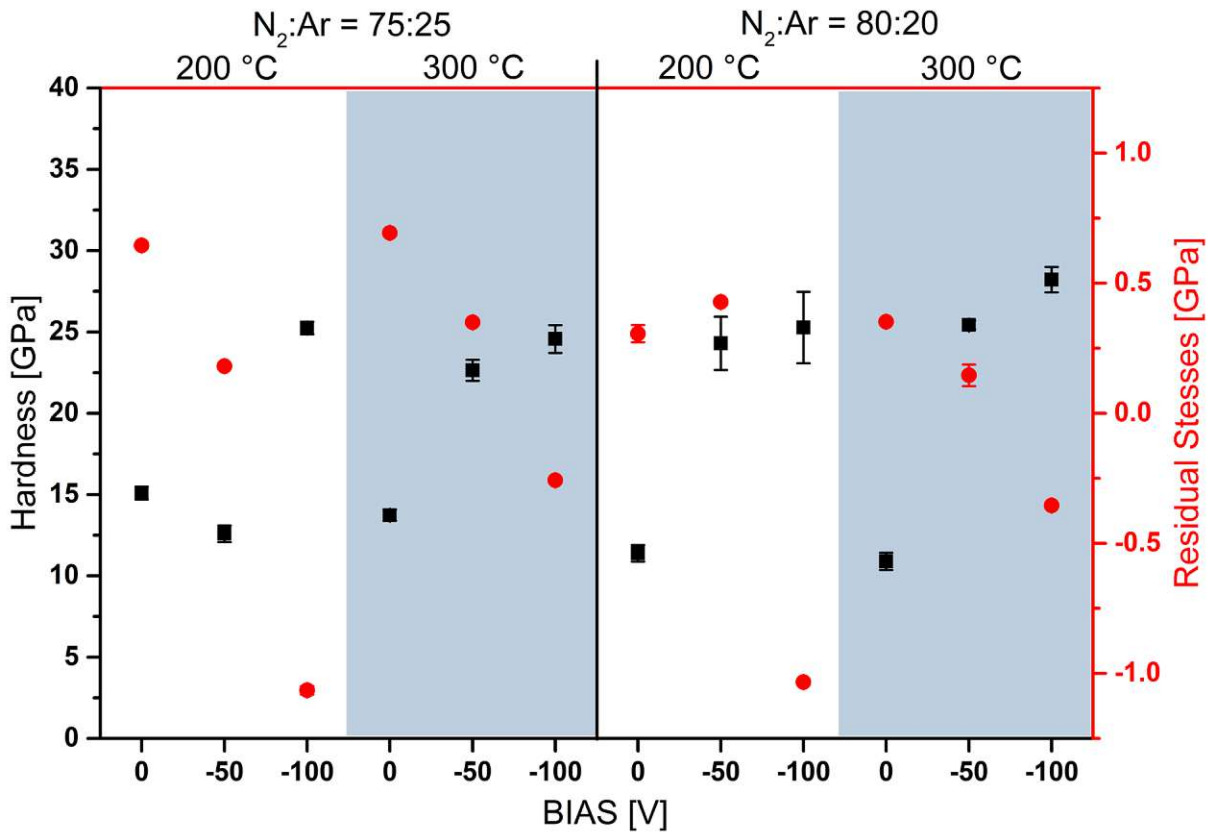

Figure 6-3: Hardness and residual stresses of the CrN coatings depending on the applied BIAS potential during the deposition process.

The mechanical properties hardness and residual stresses in the coating are two highly important characteristics for the definition of the baseline coating for the further adhesion experiments. The requirements are hardness values of around 20 GPa and compressive stresses in the coating of approx. -1 GPa. In general, residual stresses are known to show a severe impact on the adhesion properties and are therefore highly important for the adhesion.

Figure 6-3 displays the influence of the applied BIAS voltage on the hardness and the residual stress in the deposited CrN coating, which are indicated by black cubic and red circular symbols, respectively. In general, residual stresses are defined as negative if addressed to compressive stresses and positive if addressed to compressive stresses.

At floating BIAS potential, the hardness is in the range of 11-15 GPa, but at -100 V values of around 25 GPa and higher are found. The highest hardness, with 28.2 GPa, exhibits the coating deposited at 300 °C and a gas ratio of 80% N_2 to 20% Ar. Furthermore, the hardness values typically increase for higher BIAS voltages, except for 200 °C and 75% N_2. A different trend can be identified for the residual stresses. The residual stresses in the coating change from tensile (>0 GPa) to compressive (<0 GPa) stresses, for BIAS voltages higher than -50 V. At floating potential, the tensile stresses are around 0.75 GPa for 75% N_2 and 0.3 GPa for 80% N_2,

respectively. Increasing the BIAS up to -100 V results in the introduction of compressive stresses in the coating, with values of lower than -1 GPa for the CrN thin films deposited at 200 °C. At 300 °C the stresses only reach values of around -0.25 to -0.3 GPa. This can be attributed to the higher mobility of the adatoms at elevated temperatures on the surface of the substrate. Furthermore, the tensile stresses in the coatings deposited with 80% N_2 are generally lower than for the ones deposited at a 75% N_2 gaseous atmosphere. The trend of increasing hardness values at higher BIAS voltages and the introduction of compressive stresses in the coating is due to the bombardment with ions during the growth of the coating, resulting in denser and more compact films, with finer grains. This phenomenon was already described earlier (please see chapter 2.

Based on the requirements, which derive from the industrially used coatings (see chapter 5.1), the CrN films deposited at 200 °C and 300°C with an gaseous atmosphere of 80% N_2 and 20% Ar have been chosen as the baseline for the following adhesion and etching rate determination experiments. These coatings are cubic CrN, with a slightly over-stochiometric chemical composition. The residual stresses in the coating are compressive (-0.36 GPa for 300 °C and -1.03 for 200 °C, respectively). The hardness values are around 25 to 28 GPa. Although, the coating at an heater temperature of 200 °C mimics the industrial application in more detail, the coating deposited at 300 °C has been chosen too, to get a better understanding how the remaining stresses influence the different etching procedures and the adhesion properties. Later, only the coatings deposited at 200 °C heater temperature had been used, to further eliminate a possible influencing factor and to reduce the number of the individual coating runs.

6.2 Adhesion Improvement

The adhesion of a thin film on the substrate is a key factor in the sufficient use of the coating for a certain application, e.g. an injection system for an automotive application. The results of the investigations on the influence of the etching properties on the adhesion of the coating on industrially used valve pieces is shown in this chapter.

CrN, deposited at 200 °C heater temperature, was applied to all tested samples, in order to eliminate the influence of different coating properties. All coated valve pieces were tested using the industrially well-established HRC-adhesion test, an easy and fast to use analytical technique. The sample is penetrated by a Rockwell-cone indenter and the remaining imprint is classified based on certain failure categories (please see chapter 4.4). For a further characterization of the adhesion of the thin film, TEM and SEM investigations were used for selected samples.

As it can be seen in chapter 5, three different experimental setups were used to investigate the adhesion properties of the CrN coating on the valve pieces. After the first experimental setup, severe delamination on the valve pieces for all investigated etching procedures was visible. Figure 6-4 a) and b) shows the top-down view on the surface of the valve piece for argon- and Cr-ion etching, respectively. The bright spots result from the delamination of the coating, indicating a subpar adhesion of the thin film. A possible explanation could be the presence of corrosion inhabitants and other protective oils on the surface, lowering the adhesion of the coating. Therefore, a more aggressive external cleaning routine, before the etching and coating process, was established, see chapter 5.3. This routine was used for all the following samples. Furthermore, from now on, only the CrN coating deposited at 200 °C heater temperature and a gas ratio of 80% N_2 and 20% Ar, was applied for the following experiments. This further limits

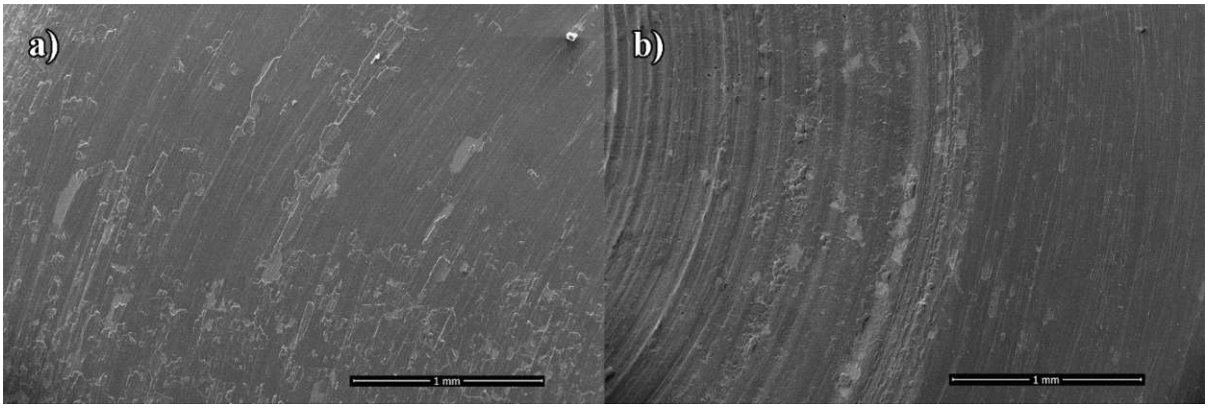

Figure 6-4: Delamination of the CrN at the 1st experimental setup for a) argon etching at -400 V BIAS, b) Cr-ion etching at -700 V BIAS.

the influencing factors on the adhesion properties of the thin film and reduces the needed coating runs for the characterization of the different etching procedures.

As already mentioned before, for the second coating run, a more aggressive cleaning routine was established, compared to the 1st experimental setup. Furthermore, the etching time was prolonged, from 10 min to 100 min. Also, the BIAS potential has been increased for all etching procedures (argon, forming gas, N_2, Cr^+). Instead of -400 V and -700 V, respectively, -1000 V was used. At the 3rd experimental setup only Cr-ion and forming gas etching procedures were conducted. These etching tests were performed only using the valve piece made of nitrided steel. All process parameters can be found in chapter 5.

6.2.1 HRC-Adhesion Tests

Figure 6-5 displays the remaining indentations after performing the HRC adhesion test for all conducted Cr-ion etching procedures, whereas Figure 6-6 shows the indentations for the etching processes using forming gas ($Ar+H_2$), argon or nitrogen as working gas.

The figures are categorized by the used BIAS configurations, differencing in either the applied BIAS potential (-400 V, -700 V and -1000 V, respectively), the BIAS mode (synchronized or DC) or the overall etching time (100 min., 120 min., 360 min.). For DC BIAS a direct current signal has been applied, whereas synchronizing mean that the BIAS signal is triggered by the HiPIMS signal at the cathode. The results for the Cr-ion etching procedures are further subdivided by the configuration of the cathode (one cathode or two cathodes equipped with Cr targets used) to which the HiPIMS signal, for the generation of the Cr^+ ions, has been applied. Furthermore, for one etching run, forming gas was used as a working gas, instead of Ar. The etching procedures were performed on the different valve pieces, to better mimic the practical application. These valve pieces are made from either hardened (highlighted with red boxes) or nitrided steel (highlighted by green boxes). After the 2nd experimental setup only the nitrided steel was used for further examinations, because it is of more interest for further application in injection pumps used at higher injection pressures (higher than 2000 bar). For each indentation the failure category (HF1-6) is stated in correspondence to the failure categories mentioned in chapter 4.4. The categories HF1 - HF4 are considered to be acceptable failures, whereas HF5 and HF6 indicate subpar adhesion properties. The picture of the indentations were taken using an optical microscope.

As mentioned, Figure 6-5, displays the results for the different Cr-ion procedures. It is observed that the adhesion properties on the nitrided steel are better than for the hardened steel. At the

two tested etching procedures (DC BIAS 100 min at -700 V and -1000 V) the adhesion properties are not acceptable, indicated by the delamination of the coating around the indentation. The area of delamination around the indentation is smaller for -1000 V than for -700 V BIAS but is still considered HF6. In contrary, no spalling, cracking or delamination could be observed for the nitrided steel, resulting in HF1. One reason for the subpar adhesion properties could be, that the external cleaning process was not suitable for the hardened steel substrate. After the cleaning, small oxidized spots had been visible. Prior to the coating process these spots had been removed (based on optical results) but could still be influencing the adhesion. Furthermore, all Cr-ion etching procedures applied to the nitrided steel are considered to be failure category HF1.

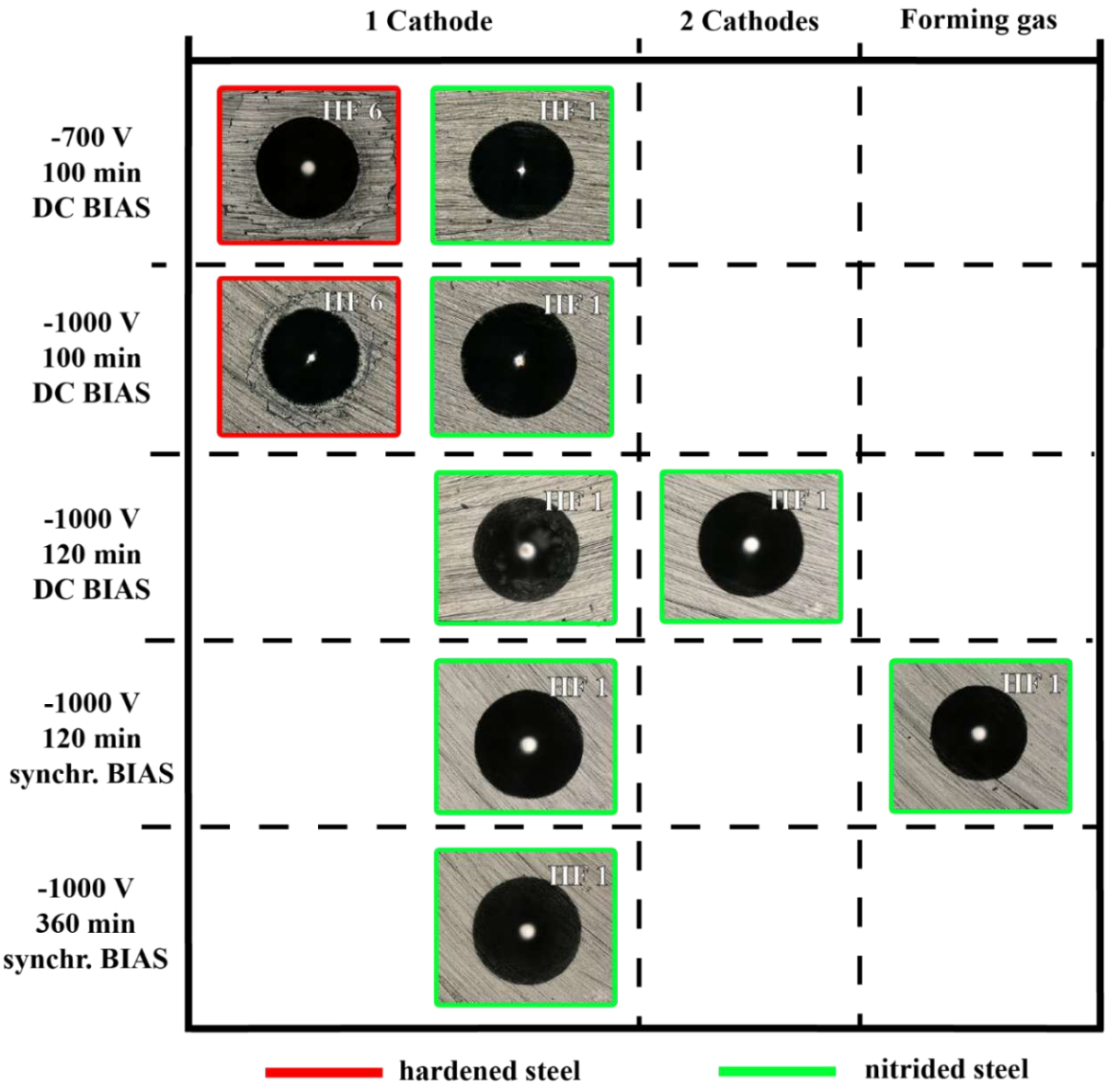

Figure 6-5: Results of the HRC-adhesion test for Cr^+-ion etching using different BIAS and cathode configurations.

These findings proof to be independent from the applied BIAS mode and the overall etching time. To validate these results, TEM investigations were conducted, see chapter 6.2.2. The samples for the further investigations were chosen based on the HRC-adhesion tests.

In Figure 6-6 the indentations of the HRC-adhesion tests for the etching procedures using different gases (or mixtures) as working gas for the etching process are displayed. Whereas the underlying etching mechanism for Argon and N_2 for cleaning of the substrate surface is through physical sputter etching, the underlying mechanism for forming gas is a combination of chemical etching (reduction of any present oxides due to the presence of hydrogen) and sputter etching. At -400 V with an etching time of 100 min. severe delamination of the coating is

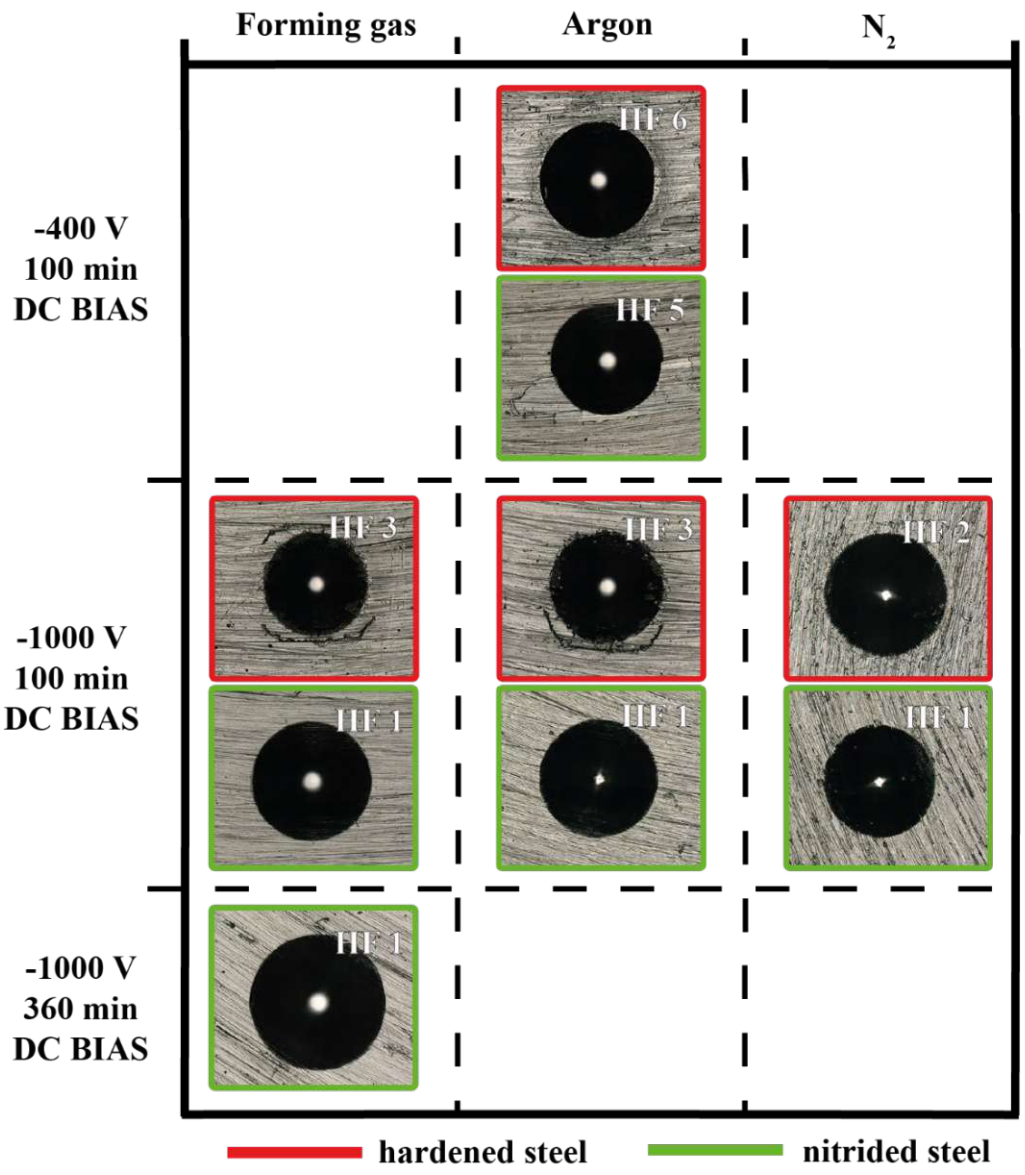

Figure 6-6: Results of the HRC-adhesion test for etching procedures using different BIAS configurations for forming gas, argon and N_2.

visible, resulting in HF6 and HF5 for the hardened and the nitrided steel, respectively. An increase in the BIAS potential up to -1000 V results in improved adhesion properties (HF3 for hardened steel and HF 1 for nitrided steel). This indicates, that at -400 V, the energy of the impinging ions is not high enough to obtain an optimal cleaning of the substrate surface. The etching procedures utilizing forming gas show a similar behaviour as the ones using argon. The failure categories HF3 and HF1 for hardened and nitrided steel, respectively, are observed. A prolonged etching time (360 min.) lead to the category HF1. For nitrogen etching categories HF2 for the hardened steel is observed, due to cracking on the edge on the indent. The nitrided steel shows an adhesion behaviour of HF1. Nevertheless, these results of N_2 and Ar etching is misleading. Observing the surface using an optical microscope reveal several areas with delamination, similar to Figure 6-4, indicating an irregular etching of the surface. This is due to differences in the etching rate of Ar and N_2 for certain contaminants, e.g. carbides and oxides. TEM analyzations of the Ar-etched samples at -1000 V and 100 min. were conducted and can be seen in chapter 6.2.2.

6.2.2 TEM investigations

The interfaces between the substrate, the Cr-interlayer and the CrN coating were investigated using transmission electron microscopy (TEM) due to the high level of maximum magnification and versatility of the analytical method, see chapter 3.2. The nature of the interfaces are of high importance to the adhesion properties of the coating. Based on the HRC-adhesion tests, different samples were chosen to be analysed through TEM. All TEM investigations followed the same routine, an example can be seen in picture Figure 6-7. STEM in HAADF mode was used to image the interface area as an overview and in detail. Furthermore, the SEAD pattern of the Cr-interlayer, as well as the CrN coating, were recorded for all tested samples. All investigated samples were prepared by focused ion beam (FIB) preparation.

Figure 6-7 shows the interface region of an Ar-etched nitrided steel sample at a BIAS potential of -1000 V. The position of the substrate, the Cr-interlayer and the CrN are indicated in the image. The SAED pictures show, that the Cr-interlayer is (110) oriented. The CrN coating has a cubic structure, with a preference in crystalline orientation of (200) and (220). This is in good correspondence to the results obtained from XRD experiments, see chapter 6.1. The SEAD pattern of all other investigated samples showed the same results, therefore, in the following images, they are not included.

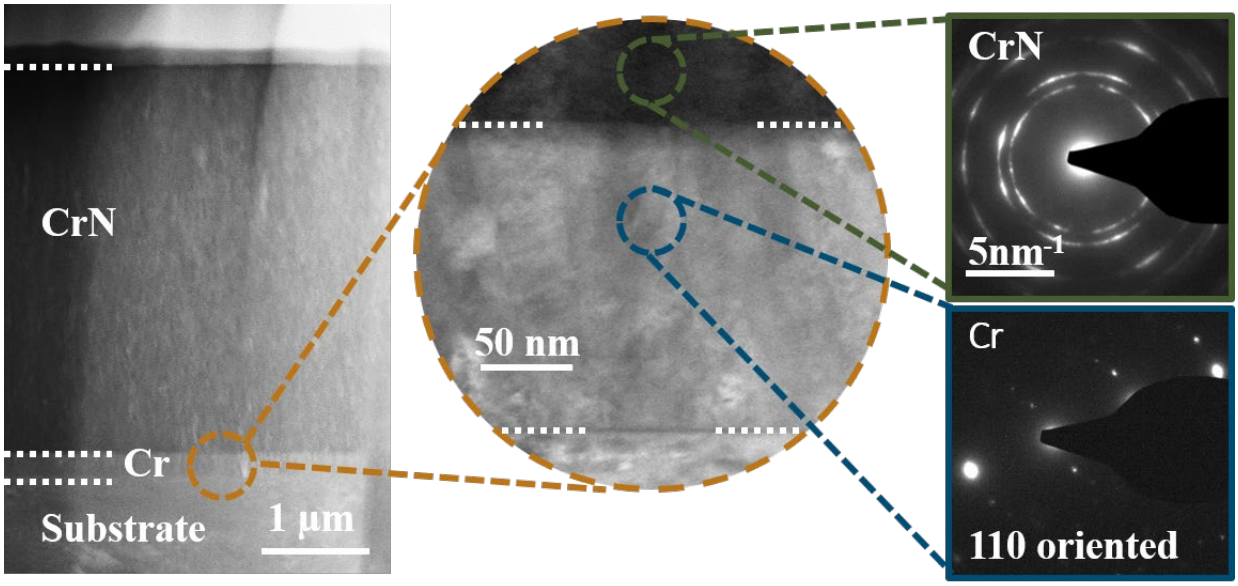

Figure 6-7: Image of Ar etched nitrided steel sample with a BIAS potential of -1000 V, with the corresponding SAED pattern of the Cr-interlayer and CrN coating.

Figure 6-8 a) – f) shows the interface of various etched samples, recorded by TEM. In the pictures, the positions of the CrN coating, the Cr interlayer and the substrate are indicated. Figure 6-8 a) and c) show the interface for hardened steel substrates, whereas d) to f) show the nitrided steel substrates. At the interface of the Ar-etched hardened steel sample surface contaminants are visible, leading to the formation of cracks and an irregular film growth and reduced adhesion of the coating onto the substrate. This can also be seen by the HRC adhesion test, where a failure category of HF6 was obtained. Using EDS shows, that the remaining

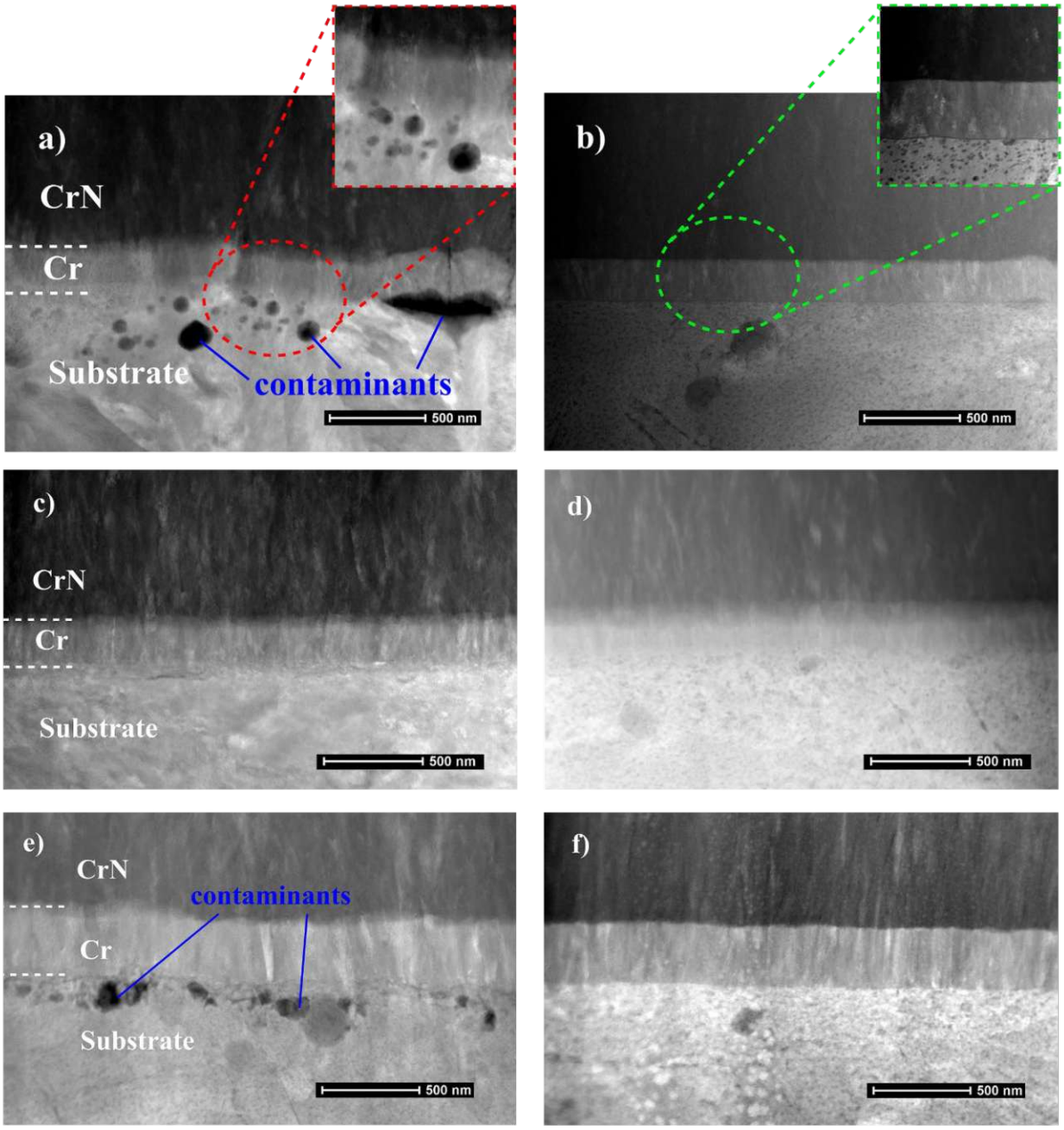

Figure 6-8: Images of the interface, recorded using TEM, of different etched samples at -1000 V BIAS a) hardened steel Ar-etched, b) nitrided steel Ar-etched at, c) hardened steel Cr-ion etched DC BIAS, d) nitrided steel Cr-ion etched DC BIAS, e) hardened steel Cr-ion etched 2 cathodes and DC BIAS, f) hardened steel Cr-ion etched synchronized BIAS.

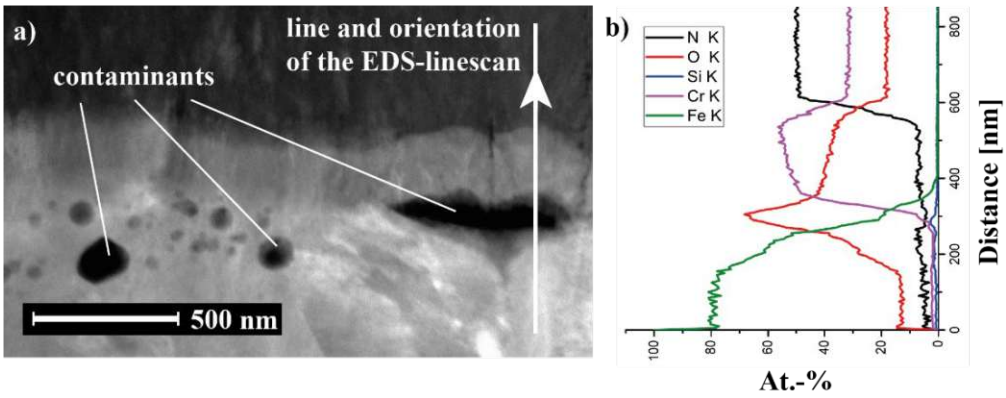

Figure 6-9: a) Cross-sectional image of an Ar-etched hardened steel sample with the indicated line and orientation of the EDS-line-scan and b) the corresponding result of the at.-% of the observed elements versus distance.

surface contaminants are most probably oxides, due to the high oxygen content found at the spots of the pollutant, see Figure 6-9 a) and b). In comparison, the nitrided sample etched with the same parameters, exhibit good adhesion properties (HF1). Nevertheless, at the interface substrate/interlayer a dark shadow can be observed but an EDS investigation showed no indication of the presence of surface contaminants.

The samples displayed in Figure 6-8 c) – f) are all Cr-ion etched samples, differencing in the used BIAS or cathode configuration. The Cr-ion etched hardened steel sample using DC BIAS (Figure 6-8 c) indicate no surface pollution, nevertheless a failure category HF6 is obtained. A reason can be, as already mentioned, the not suitable external cleaning routine for the hardened samples, resulting in the partial oxidation of the substrate. The DC BIAS etched nitrided sample (Figure 6-8 d) shows blurred interfaces, for both substrate/interlayer and interlayer/coating. This can be an indication for diffusion of Cr, creating a gradual interface, beneficial for the adhesion properties (HF1). Failure category HF 1 has been also achieved utilizing two cathodes for the creation of the Cr-ions but as it can be seen in Figure 6-8 f) surface contaminants are found at the interface region. The reason could be that the magnetic fields of the two cathodes are interfering with each other, leading to the deflection of the Cr-ions, resulting in irregular etching of the surface. However, synchronizing the BIAS potential (Figure 6-8 f) to the cathode HiPIMS signal leads to a contaminate free surface.

In summary, the HRC adhesion test can be used a first indication of the adhesion properties of the coating but further investigations of the interface should be conducted. For example, all Cr-ion etched nitrided steel substrates are categorized as HF1 but the utilization of two cathodes for the ion creation leads to irregular etching results. Furthermore, for the argon-etched hardened sample a severe amount of contaminates is present, resulting in irregular film growth and the formation of cracks.

6.3 Etching Rate Determination of Cr-Ion Etching

The etching rate is a key quality in the evaluation of the effectiveness of the entire etching process. Therefore, the determination of this value is of high importance. Due to the etching, material is removed from the surface of the samples, resulting in a loss of height or thickness, which can be measured. The etching rate is then described as the resulting etched height (difference of the sample thickness before and after the etching process) per time unit (e.g. nm/h).

To evaluate the etching rate various prepared substrates were used. As described in chapter 5.4, silicon and austenite samples, with well-known and defined properties, were placed along with the valve pieces in the sample holder. Before the deposition run, these samples were partly coated with TiO_2. This insulating layer protects the covered surface area from any influence of the etching and coating process. Afterwards, the protective TiO_2 layer is removed, leaving the

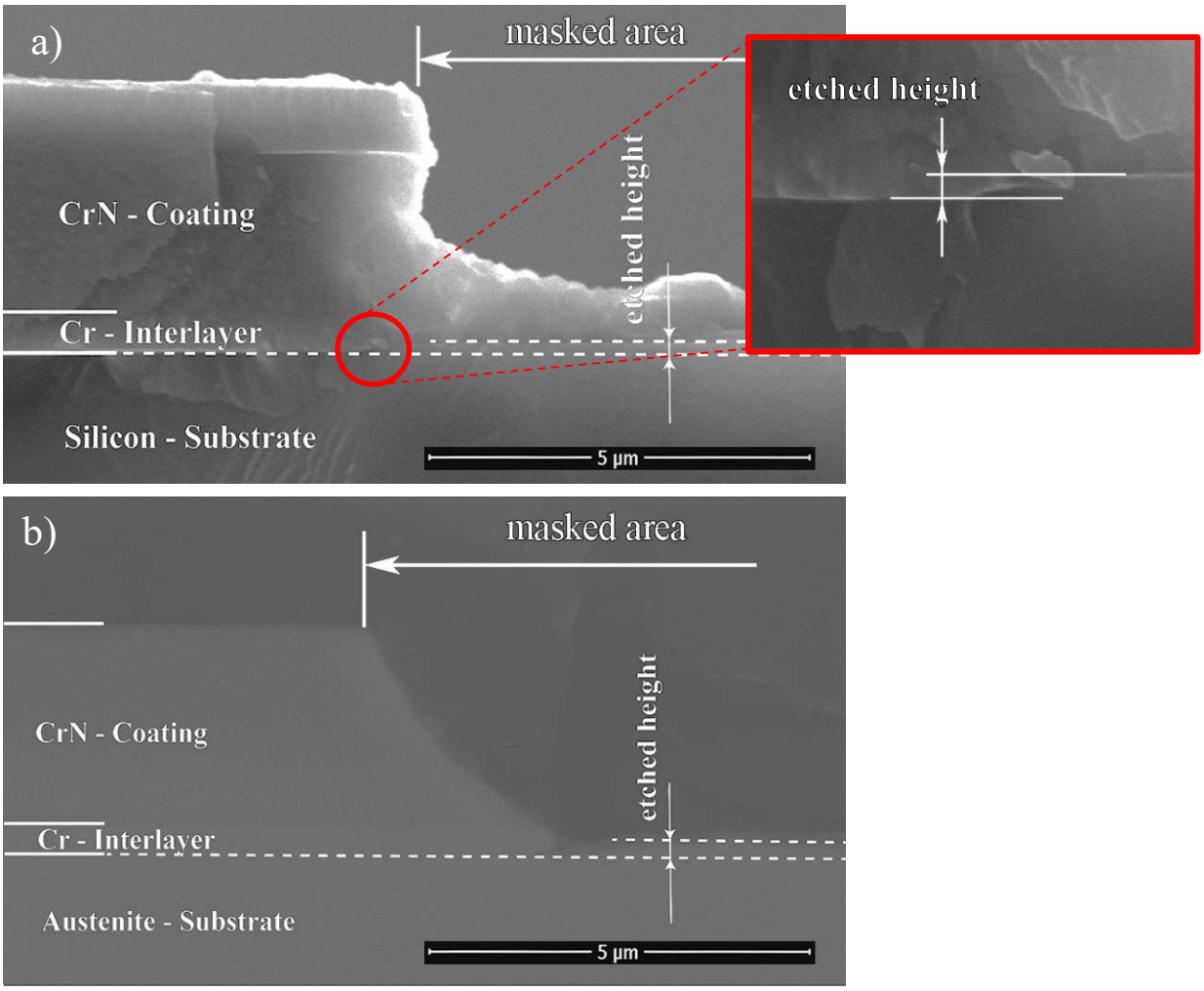

Figure 6-10: Cross-sectional images of the masked samples after Cr-ion etching using a gas mixture of Ar/H_2 and coating with Cr interlayer and CrN on a) silicon substrate, with detail of the etched height, b) austenite substrate.

unharmed substrate surface behind, which can be seen in Figure 6-10 a) for silicon and b) for austenite substrates, respectively. Scanning electron microscopy was used for the examination. The images show the samples after an etching run with a gas mixture of Ar/H_2 (forming gas) and the coating of the samples with a Cr-interlayer and a CrN thin film. The prior masked area of the sample is indicated by the edge of the CrN coating. Furthermore, for Figure 6-10 a) a detailed image of the transition from the masked to the unmasked area is given, which clearly reveals a height difference between the two zones. This difference is due to, the beforehand mentioned, removal of material by the etching process and represents the so-called etched height. All Cr-ion etching treatments show this pronounced etched height. The direct measurement of the etched height from the SEM images was possible, but not sufficient for the determination of the etching rate, due to the high uncertainty of the measurement in the nanometre scale. Therefore, the etched height was calculated using Equation (6.1). Figure 5-6 schematically illustrates these variables.

$$etched\ height = coating\ thickness - step\ height \tag{6.1}$$

The coating thickness has been measured using the cross-sectional images of the thin film examined by SEM. To determine the step height (height difference between the top of the CrN coating and the masked area) an optical profilometer was used. Figure 6-11 illustrates the step height, measured by optical profilometry, for a Cr-ion etched sample using forming gas. This height difference could have been measured using SEM, but the optical profilometer is easier in the handling, faster and results in a better resolution. The etching rate could then be calculated by dividing the etched height by the etching time, see Table 5-5.

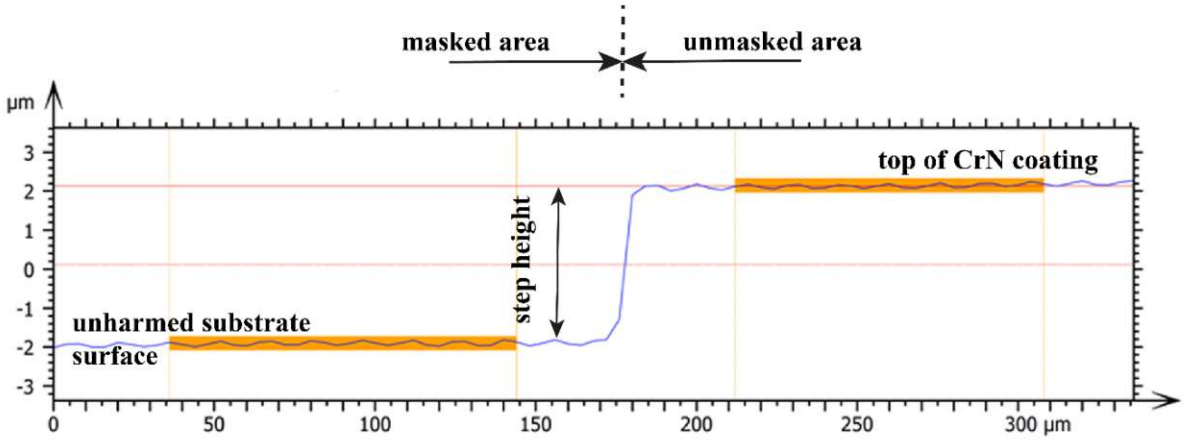

Figure 6-11: Measured step height after coating and etching for Cr-ion etching process using forming gas.

Figure 6-12 shows the etching rate (nm/h) for the tested Cr-ion etching processes on silicon and austenite substrates. Silicon substrates were used, due to their pronounced properties and easy handling regarding SEM investigations. On the other hand, the austenite samples should better mimic the behaviour of the valve pieces, due to their similarity in chemical composition and structure. The process parameters can be found in Table 5-5. The etching rates for the silicon substrates are indicated by black cubic symbols, whereas the symbols for the austenite substrates are black circles.

For the silicon substrates the etching process using a DC (direct current) BIAS signal, along with Ar as working gas (WG), shows the lowest etching rate (12.5 nm/h). Synchronizing the BIAS signal, with the HiPIMS signal producing the Cr-ions, leads to an increase in the etching rate up to 20-23 nm/h, slightly depending on the overall etching time. A similar behaviour, at least for the 2h etching run with synchronized BIAS, can be observed for the austenite substrates. The etching rate for the DC BIAS signal is 17 nm/h, compared to 16.2 nm/h for synchronized BIAS 6 h and 27 nm/h for a 2 h etching time. One explanation of this gain in the etching rate, can be that by using a synchronized BIAS potential the BIAS generator is able to withstand the hight current peaks caused by the incoming Cr-ions. The ions are only produced

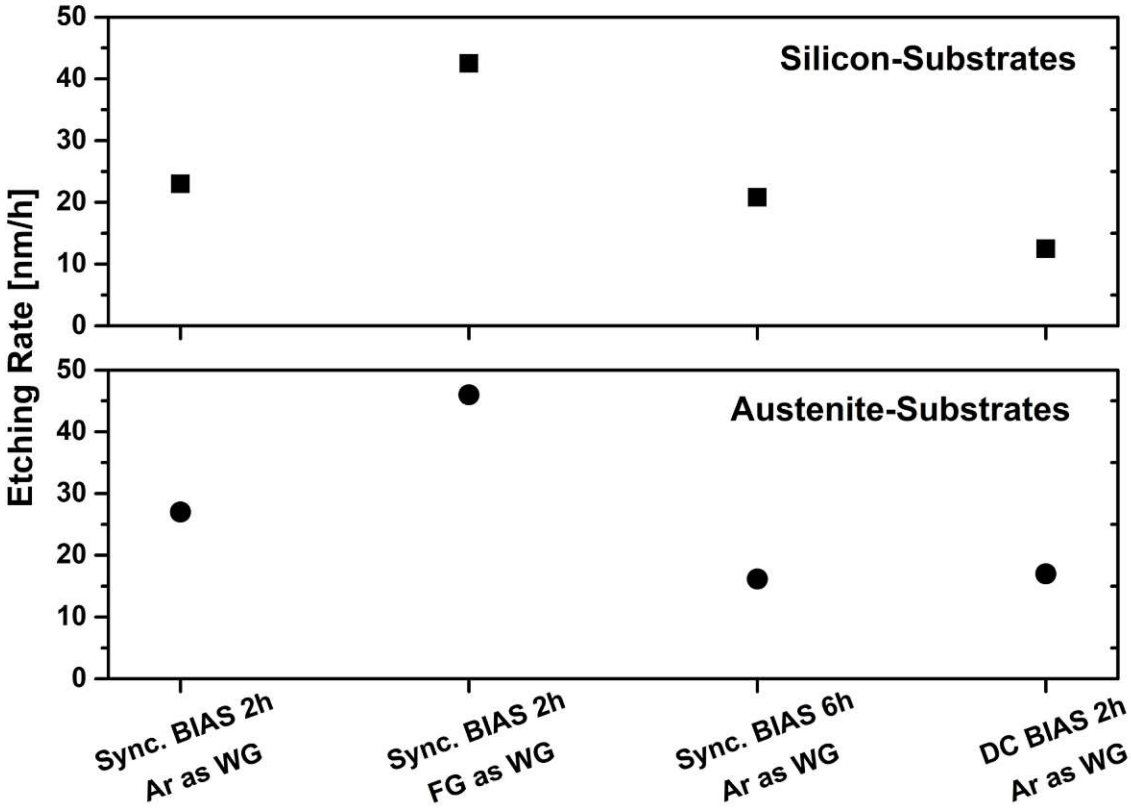

Figure 6-12: Etching rate for different Cr-ion signal etching procedures for silicon and austenite substrates utilizing argon (Ar) or forming gas (FG = Ar+H_2) as working gas (WG).

during the short pulse of the HiPIMS at the target, therefore, by synchronizing the signal of the BIAS to this pulse, a better management of the ion flux is obtained. This advanced control of the ions probably also leads to a higher bombardment of the substrate with Cr^+-ions. Furthermore, by using a synchronized signal, a more stable process is achieved, resulting in less arcing during the etching.

The highest etching rate, for both silicon and austenite substrates, is observed by Cr-ion etching utilizing forming gas (FG - 95% Ar and 5% H_2), combined with a synchronized BIAS signal. The etching rates reaches values of 42.5 nm/h for silicon substrates and 46 nm/h for austenite substrates, respectively. By using forming gas, two different etching phenomena are combined, sputter-etching and chemical-etching, so-called reactive sputter-etching. The Cr-ions bombard the surface, leading to the ejection of substrate surface atoms, whereas the H_2 reacts with surface atoms and contaminates and forms a more volatile species, which then gets removed.

Comparing silicon and austenite substrates shows, that the etching rates are in the same range for all the tested etching procedures. Therefore, for our tested material and etching systems, the substrate material is not influencing the etching rate in a distinct manner. Furthermore, of all tested etching procedures, Cr-ion etching using forming gas as working gas shows an etching rate of around 47 nm/h, whereas using only Ar as working gas 27 nm/h was the maximum. The remaining etched height was clearly visible in the pictures recorded by SEM.

6.4 Implantation Depth of Cr

As it is suggested by several studies, metal ion etching has the capability to enhance the adhesion properties of thin films. Beside the improved removal of unwanted contaminants, the main phenomena, for the increased adhesion, is the implantation of metal ions into the surface of the substrate, creating a pseudo-diffusion zone, see chapter 2.3.1 and 2.4. For the deposition of CrN films, the implantation of Cr-atoms is beneficial, especially if a Cr-interlayer is applied. To evaluate the implantation depth of the ions into the surface of the substrate matter, different approaches have been applied, which are shortly described.

A theoretical calculation has been conducted, using the SRIM (stopping and range of ions in matter) program [57], based on the work by J. F. Ziegler et al. [58]. This program calculates the stopping and range of ions at the collision of these with solid matter and based on the quantum mechanical aspects of these interactions. To verify the theoretical calculations, Cr-ion etched samples, coated with a thin, protective Mo-layer, were prepared, see chapter 5.5, and analysed using ERDA, RBS and SIMS. These three are ion beam analytical techniques, capable of determining elemental concentration depth profiles. All methods have a high sensitivity for the content of the detected species, which is even true for light elements and a high depth sensitivity. A more detailed insight of these analyse techniques is given in chapter 3.5, 3.6, and 3.7 respectively.

6.4.1 Theoretical Implantation Depth calculated using SRIM

The results of the calculated implantation depth (in Å) of Cr and Ar ions, depending on the energy of the bombarding ion (eV), is given in Figure 6-13. The calculations were conducted up to 1000 eV, because this corresponds to the highest value the BIAS generator of the used deposition plant is capable of delivering (when considering single charged ions as the main species). The rhombic symbols stand for Cr^+-ions, whereas the cubic symbols represent Ar^+-ions. The calculations were conducted for different substrate materials, each displayed by a different colour in the graph – grey for silicon (Si), blue for iron (Fe) and green for stainless steel (SS). As expected, the calculated implantation depth of all ion species is higher for silicon substates, than for iron or stainless steel. At an energy of 1000 eV, the implementation depth is up to 250 % higher (around 33 Å for Si and 13 Å for Fe and SS). The binding energy of the Fe-atoms in the structure of iron and stainless steel is higher than for Si, resulting in the difference in the implementation of Cr and Ar ions. Overall, nearly no difference can be observed between Fe and stainless steel. This can be attributed to their similarity in atomic structure and especially

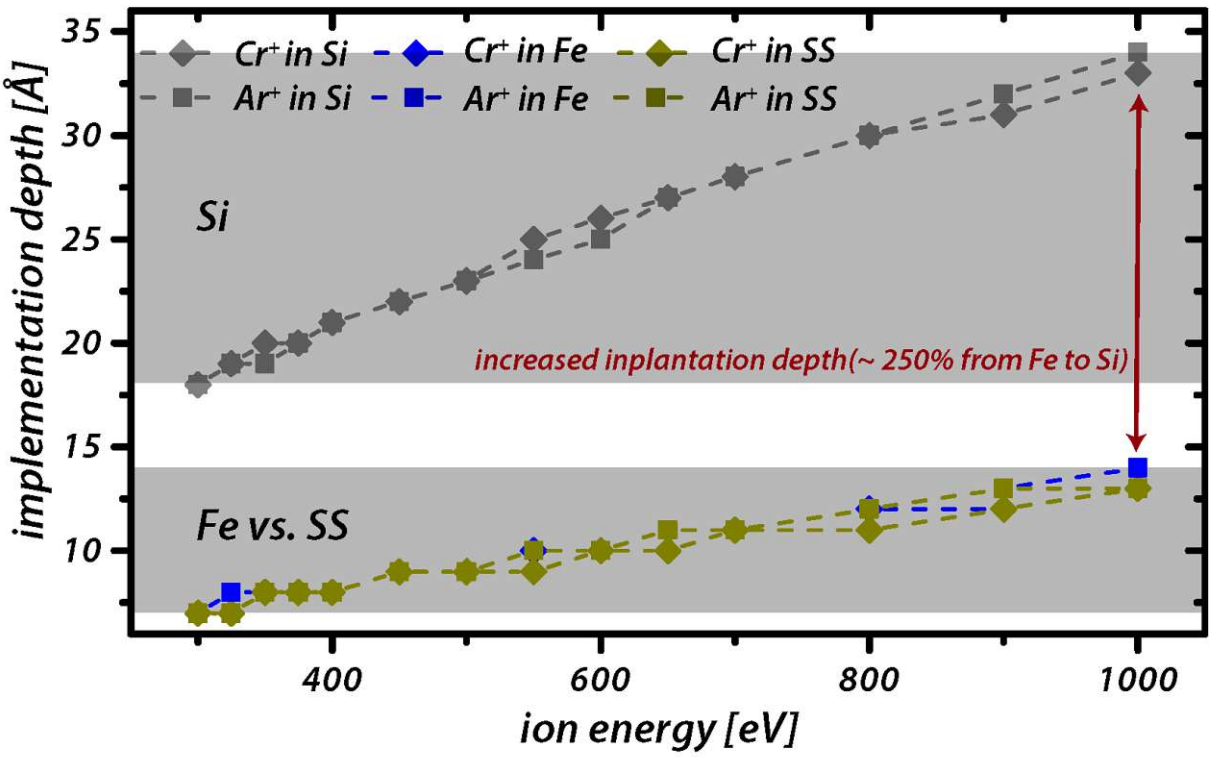

Figure 6-13: Theoretical implantation depth of Cr and Ar ions, calculated using SRIM, in silicon (Si), iron (Fe) and stainless steel (SS) substrates.

the mass of the present atoms. Furthermore, it can be seen, that the implantation depth on all tested substrates is almost independent if Ar^+ or Cr^+ ions are used. A possible explanation therefore is, that though the atomic mass of Cr (~52 u) and Ar (~ 40 u) is different, more Ar^{2+} ions are generated than Cr^{2+}, cancelling the mismatch in mass. The calculations also suggest an implantation of Cr in steel at ion energies lower than 750 eV, in contrary to already published findings, where at energies lower than this a net deposition was observed [26].

6.4.2 Implantation zone determination of Cr into austenite substrates using RBS and ERDA

The determination of the implantation zone of the Cr^+-ions into the surface of austenite samples, RBS and ERDA measurements were used. For both methods, the sample is bombarded with energetic particles, either leading to the recoil of target atoms (ERDA) or the scattering of the impinging ion (RBS).

Figure 6-14 displays the results of a RBS measurement of a Cr-ion etched austenite sample at -300 V applied BIAS potential and coated with an protective Mo-layer. The graphs display the counts versus the channel (eV/ch), which corresponds to the energy of the backscattered ions.

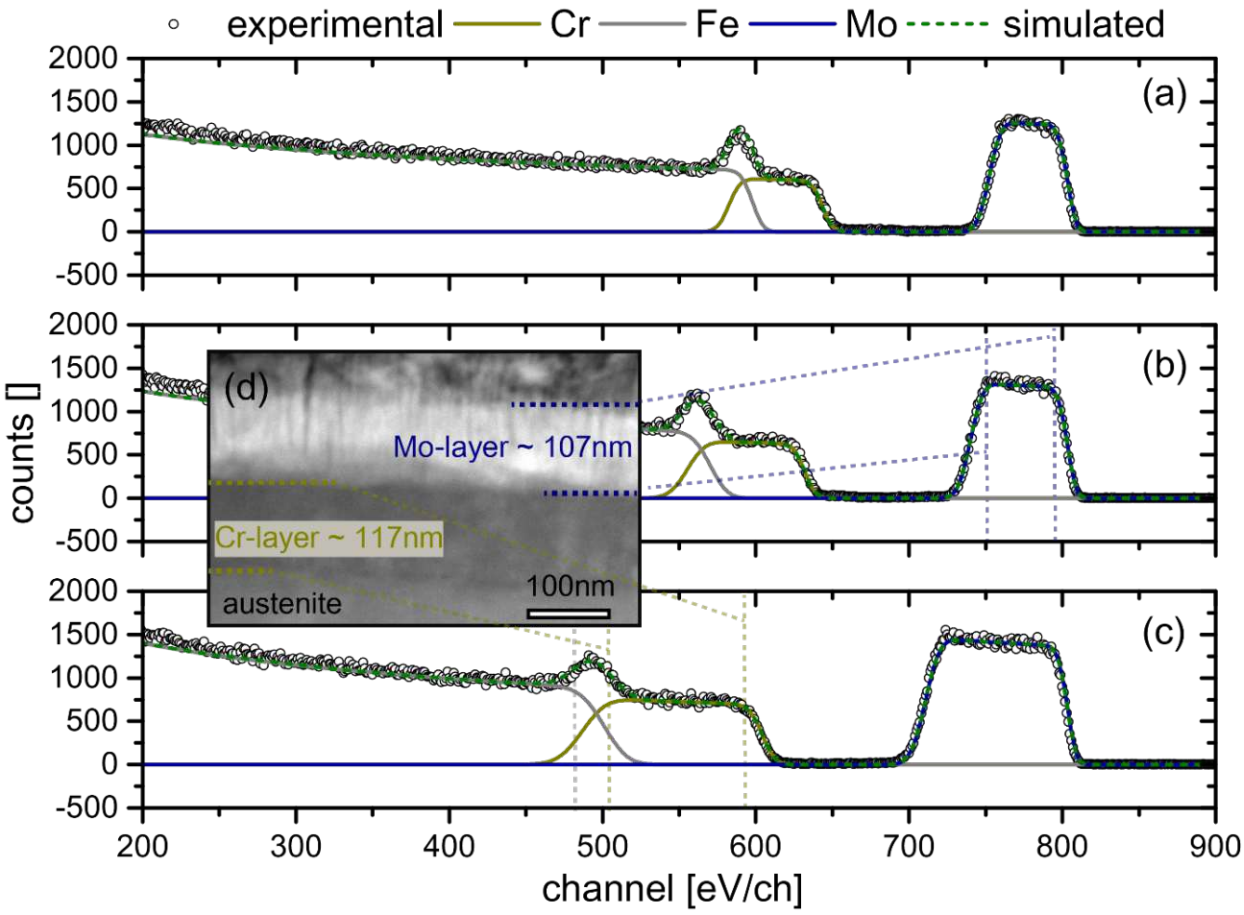

Figure 6-14: Results of the RBS measurement of a Cr^+-ion etched austenite sample at -300 V applied BIAS potential for impinging angles of a) 5°, b) 40° and c) 60°. d) shows the affiliated cross-sectional image acquired by TEM. The position of the edges of the signal are linked to the cross-sectional image by ocher lines for Cr and blue lines for Mo, respectively.

The experimentally gained data are indicated by circles, whereas the simulated data are displayed by a green dashed line. The simulated data is in consideration of the surface roughness, resulting from hand polishing of the samples prior to the coating and etching process. The present elements are indicated by ocher (Cr), grey (Fe) or blue (Mo) lines. Furthermore, the RBS measurement was conducted at impinging angles of the projectile He^+-ion of a) 5°, b) 40° and c) 60°, respectively, to enhance the resolution of the measurement. Figure 6-14 d) displays the cross-sectional image of the corresponding sample observed by TEM. The same measurements have been conducted for austenite samples etched at -700 V and -1000 V, respectively.

As it can be seen in Figure 6-14 a) to c), higher impinging angles, lead to broadening of the signals, due to the extended distance the scattered ions have to travel to reach the detector. This has to be considered at the following calculation of the thicknesses of the individual layers. The signals for Cr and Fe are overlapping, because of their similarity in atomic number *Z*. As

Table 6-1: Thickness of the different layers of austenite etched samples at -300 V, -700 V and -1000 V BIAS

BIAS potential [V]	Thickness [nm]	
	Mo	Cr
-300	107	117
-700	109	25
-1000	107	0

already mentioned in chapter 3.7, from the width of the signal for one element, the depth, at which the ion had been scattered at this sort of atom, can be calculated. The resulting thickness of the individual layers, for all analysed BIAS potentials, can be seen in Table 6-1. Overall, with improved BIAS potentials, the thickness of the deposited Cr-layer, during the etching process, declines. At the etching process using a BIAS voltage of -300 V a 107 nm thick Cr-layer can be observed, at -700 V only a 25 nm thin film is deposited, whereas at -1000 V no deposited Cr is detected. This result is in good agreement with previously published findings, where a net etching rate could only be observed for BIAS potentials greater than -750 V [26]. The Mo-layer, only deposited as a protective and reference layer, is in the range of 107 to 109 nm for all different applied BIAS potentials. All these results of the observed layer thicknesses could be validated by TEM investigations, please see Figure 6-14 d).

Based on the results of the RBS investigations, ERDA measurements of these samples were conducted, with the goal do determine an implantation zone of Cr-ions into the austenite substrate. The RBS investigations show that for a BIAS potential of -1000 V no Cr-layer is deposited.

The findings of the ERDA measurements can be seen in Figure 6-15 a) to c). The graphs show the atomic content (atomic-%) of Fe (grey), Mo (blue) and Cr (ocher) versus the depth (presuming 10^{15} atoms /cm^2). The measurements were conducted for samples etched at different BIAS voltages – a) -1000 V, b) -700 V and c) -300 V. Figure 6-16 gives an detailed view of the 1st derivative of the implantation zone for the sample etched at -1000 V. The position of the detail is indicated in Figure 6-15 a).

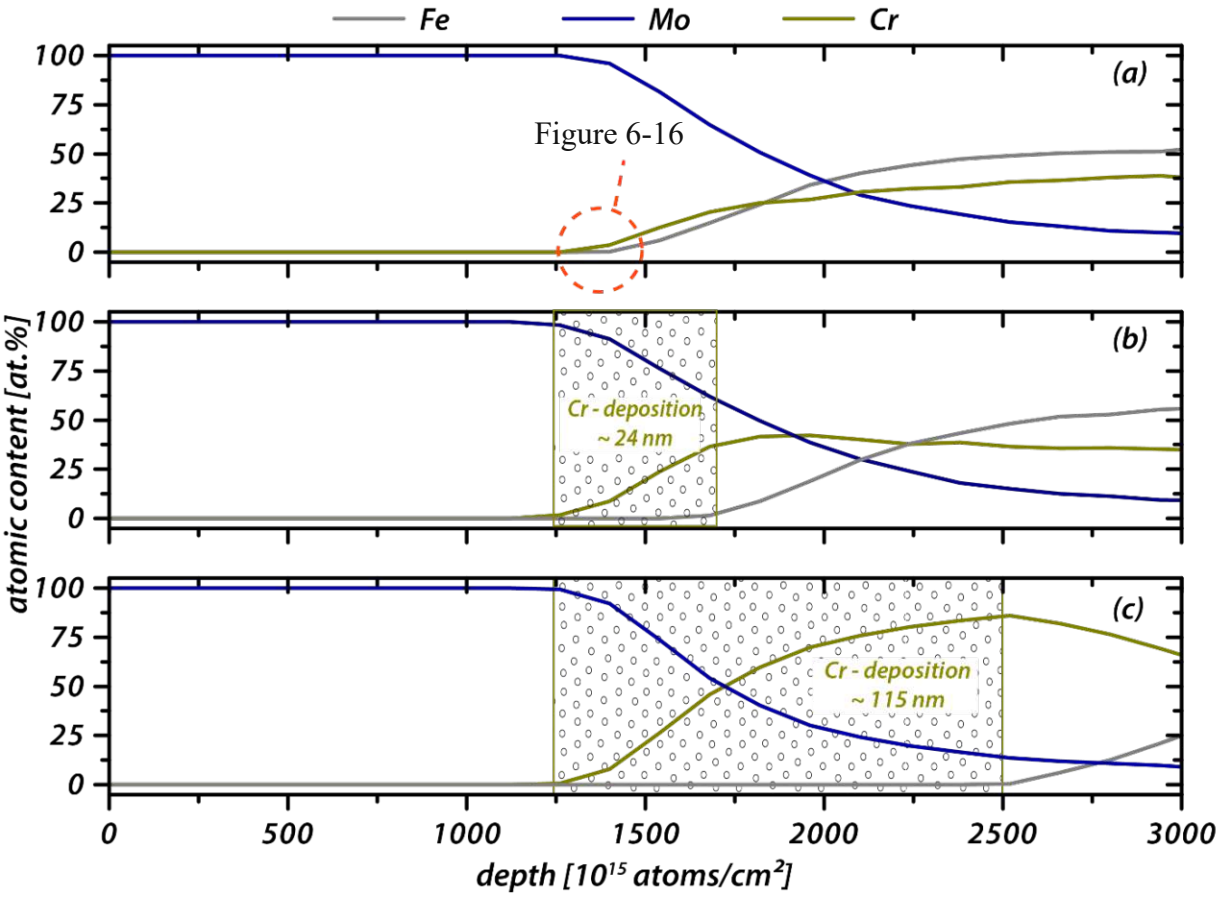

Figure 6-15: Graphs of the atomic content versus the depth, of Cr^+-ion etched austenite samples, gained by ERDA. investigations for different applied BIAS potentials a) - 1000 V, b) -700 V and c) -300 V. For -300 V and -700 V the thickness of the deposited Cr-layer is indicated.

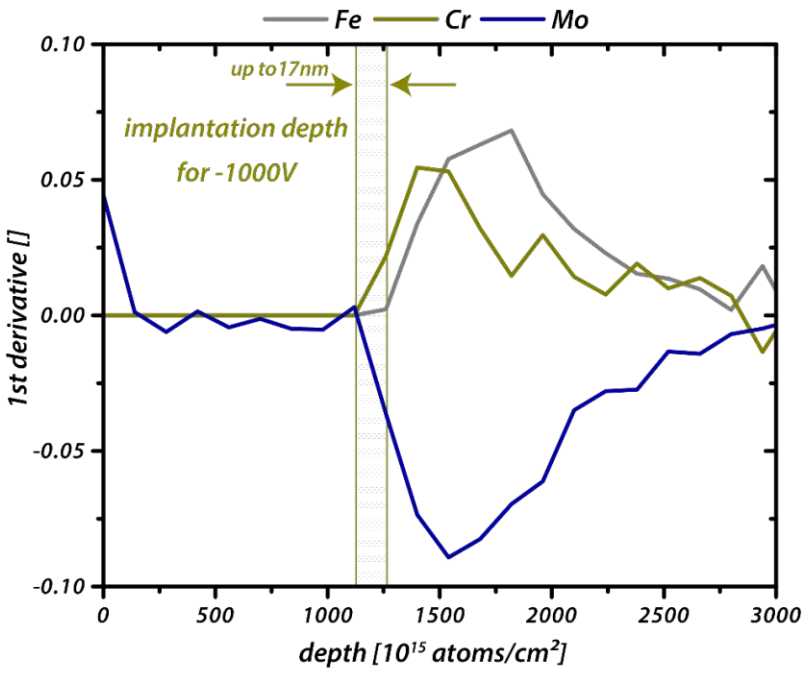

Figure 6-16: Detail of the 1st derivative of the Cr^+-ion etched austenite sample at -1000 V. The presumed implantation zone of Cr-ions into the surface is indicated.

The ERDA measurments for the etched samples at -300 V and -700 V applied BIAS potential show a net deposition of Cr during the etching process, see Figure 6-15 b) and c). The thicknes of the observed Cr-layer is 117 nm at -300 V and 25nm at -700 V, respectively. These thicknesses can be seen in Figure 6-15 b) and c). At a depth of around 1250 (10^{15} atoms/cm^2) the Cr signal (green) starts to grow, whereas no signal of Fe (grey) is detected. Simultaniously, the Mo signal is declining. These are indications of the formation of a pure Cr-layer. The results, of the deposition of a Cr layer, are in good agreement with the results of the RBS and TEM observations discussed earlier in this chapter.
Contrary, Figure 6-15 a) shows the growth of the Cr and Fe signal with different slops, at the coexisting decline of the Mo-signal. Therefore a detailed insight of the 1st derivative is given in Figure 6-16. It can be seen, that at the start of the decline of the Mo signal, the Cr curve exhibits an steep growth. Furthermore, a Fe signal can be detected but with an flatter slope. The simultaneous detection of Fe and Cr, accompanied with the difference in the slopes of the curves, indicates the implementation of Cr into the surface of the Fe substrate. That no Cr was deposited at -1000 V could also be obsered from the RBS measuements, see Table 6-1. After this roughly 17 nm thick implementation zone, the slopes of the Fe and Cr signals are in the same range. Therefore no assumption of the implamantation further than 17 nm is possible, due to Cr-content of the substrate itself.

The results obtained by RBS and ERDA, along with TEM investigations, for the austenite samples etched at different BIAS potentials are in very good agreement to each other. At -300 V RBS and TEM analyses revealed the depositon of a 117 nm thick Cr-layer (Figure 6-14), which could also be observed by ERDA, where the resulting thickness of the Cr-layer is 115 nm. Furthermore, at -700 V the found thicknesses of the Cr-layer are 25 nm at RBS and 24 nm at ERDA, respectively. For an applied BIAS potential of -1000 V, RBS revealed no deposition of a Cr-layer. Combined with the results obtained by ERDA, an ~17 nm deep implementation of Cr into the Fe surface is detected. Therefore, BIAS potentials greater than -700 V are needed to obtain an etching of the surface, beeing in good agreement with literature, where an value of -750 V BIAS for steel substrates is suggested [26]. A potential error for the ERDA measurements could be, that for the calculation of the depth perfectly dense coatings were assumed, which is not entirely the case for PVD deposited coatings.

6.4.3 Implantation zone determination of Cr into Si-substrates using SIMS

For the determination of the implantation depth of Cr into the surface of Si substrates, SIMS was used. Energetic ions bombard the surface of the specimen, causing a collision cascade at the surface of the sample and leading to the emission of particles (neutrons and secondary ions). The secondary ions are then detected by a mass analyzer.

The results of the implementation zone determination of the Cr^+-ion etched silicon samples can be seen in Figure 6-17. The graphs display the intensity of the detected ion species, versus the sputtering time (s). The different ion species are presented by either ocher (Cr^+), grey (Si^+) and blue (Mo^+) lines. The measurements were conducted for samples etched at applied BIAS potentials of a) -1000 V, b) -700 V and c) -300 V. For a more detailed insight, the 1st derivative of the SIMS-measurements is given in Figure 6-18. Furthermore, the cross-sectional image obtained by TEM, of a silicon sample etched at an applied BIAS potential of -300 V is shown in Figure 6-19.

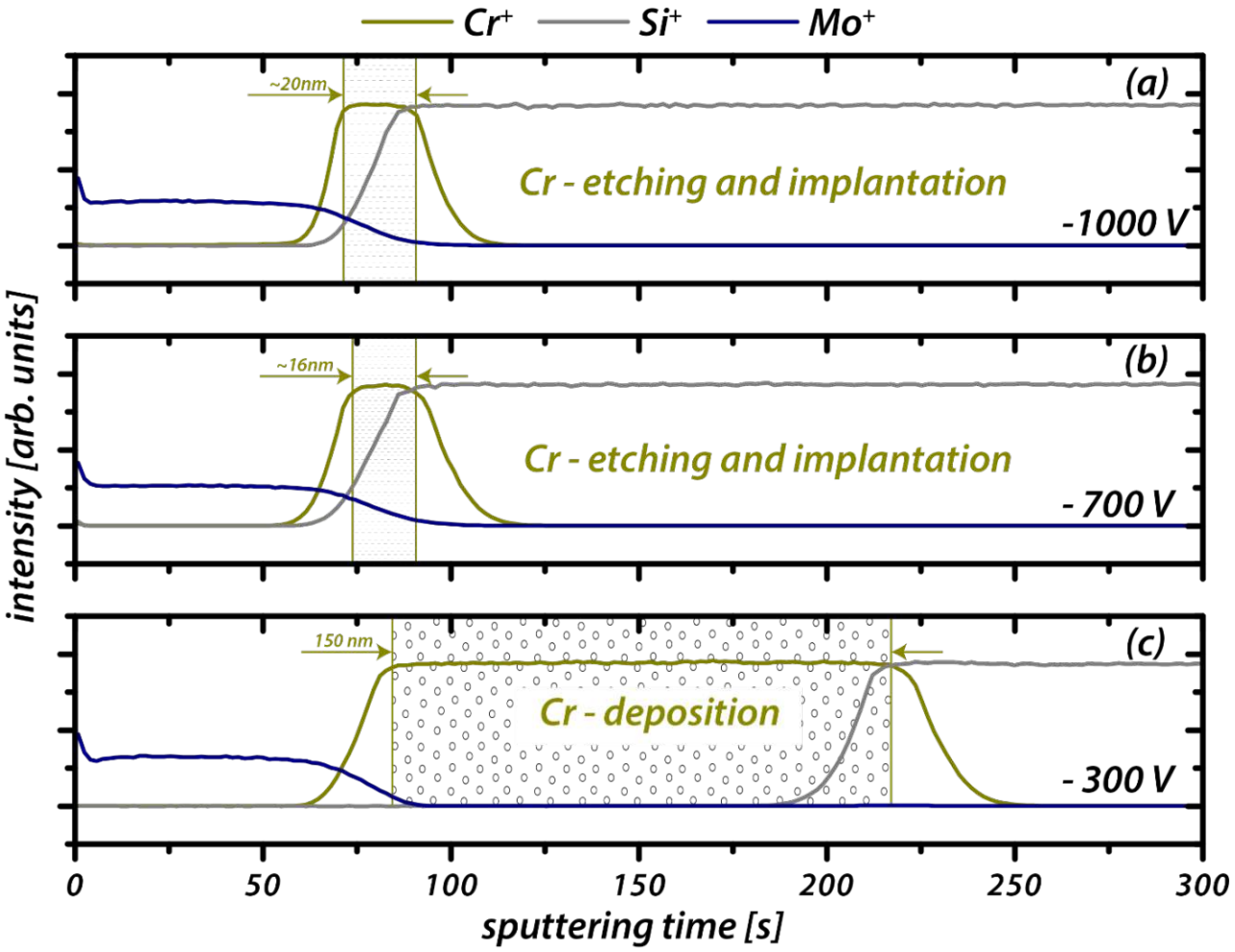

Figure 6-17: SIMS-measurements of the intensity versus the sputtering time of Cr^+-ion etched silicon substrates at BIAS potentials of a) -1000 V, b) -700 V and c) -300 V.

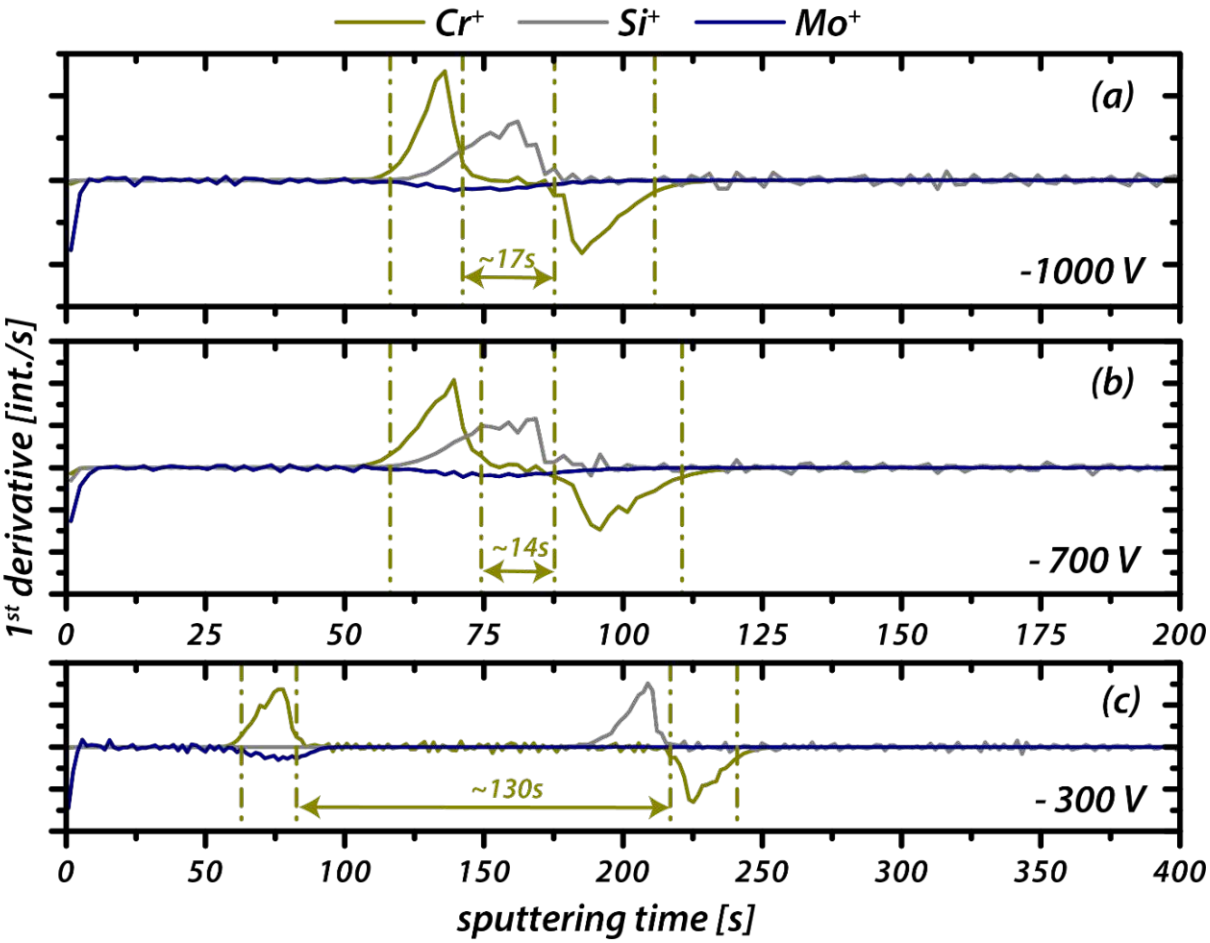

Figure 6-18: 1st derivative of the SIMS-measurements illustrated in Figure 6-17 of Cr^+-ion etched silicon substrates at BIAS potentials of a) -1000 V, b) -700 V and c) -300 V.

For the evaluation of the SIMS-measurements the sputtering yield of Cr has to be determined. Therefore, a cross-sectional image of the silicon sample etched at -300 V was analysed using TEM, Figure 6-19. The thickness of the resulting Cr-layer (150 nm) was measured and linked to the sputtering time (130 s) obtained by SIMS, see Figure 6-17 c) and Figure 6-18 c). The resulting sputtering time is the time period for which the Cr-signal has a maximum, linear trend. This corresponds with a value for the 1st derivative of zero, see Figure 6-18. From the combination of SIMS-measurements and TEM investigation it is known that a sputtering time of 130 s is equal to a 150 nm thick Cr-layer. Based on this, the sputtering yield of Cr, and therefore the depth information of Cr can be calculated for the SIMS measurements.

The SIMS-measurement seen in Figure 6-17 c) clearly shows the deposition of a Cr layer on top of the silicon substrate. At a sputtering time of around 60 s the Cr signal starts to grow, whereas the Mo-signal declined, and the Si-signal is zero. Around 80 seconds, the Cr signal is on it's maximum until a sputtering time of 210 s, where also the Si-signal reaches the maximum

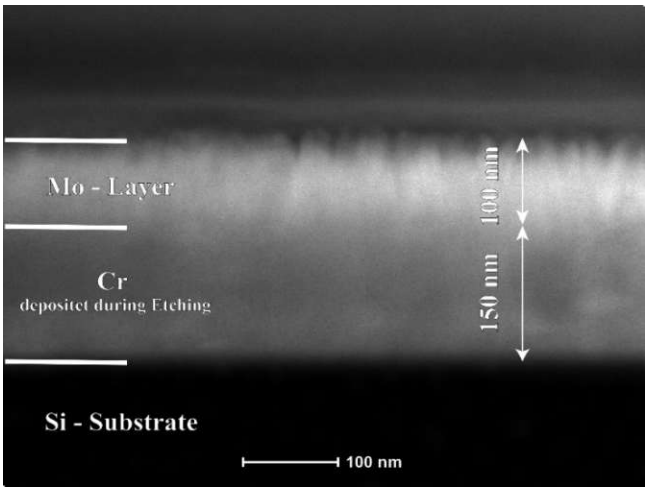

Figure 6-19: Cross-sectional image obtained by TEM of a Cr^+-ion etched Si-sample at an applied BIAS potential of - 300 V.

value. This absence of the Si-signal, until the decline of the Cr-signal, indicates the deposition of a Cr-layer.

A different trend can be observed for the Si-samples etched at -700 V and -1000 V, respectively (see Figure 6-17 a) and b)). At around 60 s, when the Mo-signal starts to decline, the Si- and Cr- signals are growing simultaneously, but with different slopes. The Cr- signal exhibits a steeper slope, therefore it reaches the maximum value before the Si. When the Si signal reaches the maximum, the Cr starts to decline. The presence of both signals concurrently, combined with the difference in intensity, indicates an implantation of the Cr into to Si surface at BIAS potentials of -700 V and -1000 V. The time periods, for which the Cr-signal reaches the maximum, are 14 s for -700 V and ~17s for -1000 V. The corresponding implantation depths are 16 nm for -700 V and 20 nm for -1000 V, respectively.

The SIMS-measurements of the Si-samples etched with different BIAS potentials clearly show the dependency of the implantation of Cr into the surface on the BIAS potential (and therefore the ion energy). At -300 V a net deposition of a Cr-layer of 150 nm thickness could be observed, whereas at -700 V and -1000 V an implantation zone of 16 nm and 20 nm thickness, respectively, could be seen. An error could result from the similarity of the sputtering yield of Cr and Fe, due to their similar masses. Furthermore, all calculations for the implantation zone are based on the deposition of the Cr-layer at -300 V, which could result in certain inaccuracies.

7 Summary and Conclusion

The goal of this thesis was to enhance the adhesion properties of a CrN thin film on heavily loaded steel parts, e.g. the injection valve, used in the automotive industry. At first a baseline CrN coating for further adhesion tests was determined using SEM, XRD, optical profilometry and nanoindentation. The baseline thin film was then chosen based on the properties of industrially used CrN coatings. To enhance the adhesion properties of the CrN, several experimental setups, with a variation of the etching procedure (Ar, N_2, Ar+H_2, Cr-ion), were conducted. The adhesion properties had been analysed using HRC-adhesion tests and TEM-investigations. Since Cr-ion etching proofs to be a very promising method, the etching rate and the implantation depth of the Cr into Si and austenite substrates were determined using ERDA, RBS and SIMS investigations, respectively. Furthermore, a calculation of theoretical implantation depth was conducted using SRIM [57].

With respect to the requirements set by the industrially used coating, the CrN thin film deposited at heater temperatures of 200 °C and 300 °C, a gaseous atmosphere of 80% N_2 and 20 % Ar and -100 V applied BIAS potential had been chosen as a baseline coating for the further adhesion experiments. EDS measurements revealed a slightly over-stochiometric chemical composition with regards to N_2 (51-53 at-% N_2 to 47-49 at-% Cr). The XRD-measurements revealed that the applied BIAS potential highly influences the resulting structure of the thin film. At a floating BIAS potential, a multi-phased CrN coating (h-Cr_2N, c-CrN) was observed, whereas at -100 V a columnar, single phased c-CrN, with a preferred orientation of (200), was detected. This can also be seen in the resulting deposition rates, which are higher at a floating BIAS potential, due to the higher quantity of more voluminous Cr_2N in the thin film. The residual stresses in the coating are compressive (-0.36 GPa for 300 °C and -1.03 for 200 °C, respectively) and the hardness values are around 26 GPa to 28 GPa, which is in good agreement to the industrially used CrN coating.

The adhesion of the thin film onto the used steel substrates (nitrided steel and hardened steel) had been determined using HRC-adhesion tests. Based on these results, samples had been chosen which are then examined in more detail by TEM investigations. All nitrided steel samples etched by Cr-ion etching exhibit excellent adhesion properties (HF1), whereas the hardened steel samples show poor adhesion HF6. One reason of the subpar adhesion properties could be, that the external cleaning process was not suitable for these samples. After the

cleaning process, small oxidized spots had been visible. These spots had been removed prior to coating and etching but could still influence the adhesion. Overall, an increase in the applied BIAS potential during the etching, as well as the synchronization of the BIAS potential to the HiPIMS signal, lead to improved adhesion of the coating. Contrary, the utilization of two cathodes for the generation of the Cr-ions, results in the existence of surface contaminations and cavities. These could also be observed for the other samples showing subpar adhesion properties.

For the etching rate determination only the Cr-ion etching procedures had been considered. Comparing Si and austenite substrates show that the etching rate, for all tested etching procedures, is in the same range and therefore almost no substrate influence is detected. The highest etching rate (47nm/h) exhibits a Cr-ion etching process utilizing forming gas ($Ar+H_2$) as a working gas. The combination of physical sputter etching (Ar) and chemical etching (H_2) results in this high etching rate. The Cr-etching processes only using Ar showed etching rates of between 12 nm/h (DC-BIAS) and 23 nm/h (synchronized BIAS). SEM investigations of the transition zone of the masked and unmasked area clearly revealed a height difference between these parts of the sample. The measured height differences, by using the recorded SEM pictures, are in good agreement to the calculated values.

The Cr-ion etched austenite samples had been investigated using a combination of RBS, ERDA and TEM. At -300 V RBS, ERDA and TEM analysed revealed a net deposition of a 115 nm-117 nm thick CrN film. By applying -700 V, the deposited Cr layer exhibits a thickness of 24 nm-25 nm, whereas at -1000 V an ~17 nm deep implantation zone of Cr into the Fe surface could be observed. These results show, that an BIAS potential higher than -700 V is needed to obtain an net etching of the surface, which is in good agreement to literature data, where an value of -750 V is suggested [23,26]. An error in the calculation of the implementation depth and the layer thickness, respectively, could be that perfectly dense coatings were assumed, which is not true for PVD deposited thin films.
The SIMS investigations of the Cr-ion etched silicon substrates clearly show the same dependency on the BIAS potential as the Cr-ion etched austenite substrates analyzed by RBS and ERDA. At -300 V a deposition of a ~150 nm thick Cr-layer could be observed, whereas at -700 V and -1000 V an implementation of the Cr-ions could be detected. The resulting implementation zones are 16 nm for -700 V and 24 nm for -1000 V, respectively. All these values were based on deposited Cr-layer at -300 V BIAS. This layer was measured using TEM

and referred to the sputtering time of the SIMS-measurement, which could result in certain inaccuracies. Furthermore, an error could result from the similarity of the sputtering yield of Cr and Fe, due to their similar atomic numbers *Z*.
A comparison of results for the Si and austenite samples show, that the implementation of the Cr-ions into the specimen surface is depending on the used substrate material. For Si substrates an implantation could be observed at a BIAS potential of -700 V, whereas for the austenite substrate a net deposition was detected. Furthermore, at -1000 V, a deeper implantation of the Cr could be noticed. This dependency could result from the binding energy of the lattice atoms, which is weaker in the case of the Si lattice.

This study clearly shows that the adhesion properties of an applied thin film strongly depend on the etching procedure. Especially Cr-ion etching and forming gas-etching, i.e. a combination of both, has the potential to further increase the application range of CrN coatings. The bombardment with atoms of relatively high mass (Cr and Ar) during Cr-ion etching, along with the implantation of Cr, results in excellent adhesion properties. Nonetheless, further investigations of the Cr-ion etching process should be conducted with a variation of further process parameters. Especially the HiPIMS signal for the creation of the Cr^+-ions and the synchronisation of the BIAS potential could be further analyzed and optimized to obtain an ideal ion flux to the substrate. Also, different working gases like xenon (already in use for advanced applications) should be considered, due to the higher mass of the atom, resulting in better etching/sputtering results. The use of Xe was advised for this thesis but neglected due to the high costs of Xe.

The implantation of the Cr ions during Cr-ion etching was already investigated in various studies [23,26,59] but the underlaying analytical methods and criteria are not ideal. In contrary, to determine the implementation in this study, only depth sensitive analytical methods (RBS, SIMS, ERDA) were used, which results in a more detailed insight of the implantation.

Bibliography

[1] Environmental aspects of the automotive industry | Internal Market, Industry, Entrepreneurship and SMEs, (n.d.). https://ec.europa.eu/growth/sectors/automotive/environment-protection_en (accessed December 16, 2019).

[2] P. Nieuwenhuis, P. Wells, P. Nieuwenhuis, P. Wells, Introduction, Automot. Ind. Environ. (2003) 1–14. doi:10.1016/B978-1-85573-713-6.50004-4.

[3] S. Wan, J. Pu, D. Li, G. Zhang, B. Zhang, A.K. Tieu, Tribological performance of CrN and CrN/GLC coated components for automotive engine applications, J. Alloys Compd. 695 (2017) 433–442. doi:10.1016/J.JALLCOM.2016.11.118.

[4] Y.-W. Chung, Introduction to materials science and engineering, CRC, Boca Raton, Fla. [u.a.], 2007.

[5] K.-H. Habig, Lexikon Werkstofftechnik, in: H. Gräfen (Ed.), 2nd ed., Springer-Verlag Berlin Heidelberg, Düsseldorf, 1993: p. 1028.

[6] W. Seidl, Werkstofftechnik, 9th ed., Hanser, München, 2012.

[7] D.M. Mattox, Handbook of Physical Vapor Deposition (PVD) Processing (Second Edition), 2nd ed., William Andrew Publishing, Boston, 2010.

[8] S. Berg, T. Nyberg, Fundamental understanding and modeling of reactive sputtering processes, Thin Solid Films. 476 (2005) 215–230. doi:10.1016/J.TSF.2004.10.051.

[9] P.M. Martin, Handbook of Deposition Technologies for Films and Coatings: Science, Applications and Technology, Elsevier Science, 2009.

[10] R.A. Haefer, Oberflächen- und Dünnschicht-Technologie : 1. Beschichtungen von Oberflächen, Springer, Berlin [u.a.], 1987.

[11] W.D. Westwood, Sputter deposition (AVS Education Committee book series), New York, 2003.

[12] H. Adachi, K. Wasa, I. Kanno, H. Kotera, Handbook of sputter deposition technology; fundamentals and applications for functional thin films, nano-materials and MEMS, (2012).

[13] K. Wasa, 3 - Sputtering Systems, in: K. Wasa, I. Kanno, H. Kotera (Eds.), Handb. Sputtering Technol. (Second Ed., Second Edi, William Andrew Publishing, Oxford, 2012: pp. 77–139. doi:https://doi.org/10.1016/B978-1-4377-3483-6.00003-6.

[14] U. Helmersson, M. Lattemann, J. Bohlmark, A.P. Ehiasarian, J.T. Gudmundsson, Ionized physical vapor deposition (IPVD): A review of technology and applications,

Thin Solid Films. (2006). doi:10.1016/j.tsf.2006.03.033.

[15] J.S. Colligon, Energetic condensation: Processes, properties, and products, J. Vac. Sci. Technol. A. 13 (1995) 1649–1657. doi:10.1116/1.579746.

[16] J.T. Gudmundsson, N. Brenning, D. Lundin, U. Helmersson, High power impulse magnetron sputtering discharge, J. Vac. Sci. Technol. A. 30 (2012) 30801. doi:10.1116/1.3691832.

[17] J. Keraudy, D.T. Nguyen, A. Ferrec, P.-Y. Jouan, Comparison Between DC and HiPIMS Discharges. Application to Nickel Thin Films, in: H. Fujita, D.C. Nguyen, N.P. Vu, T.L. Banh, H.H. Puta (Eds.), Adv. Eng. Res. Appl., Springer International Publishing, Cham, 2019: pp. 196–203.

[18] B.A. Movchan, A.V. Demchishin, Fizika Metallov I Metallovedenie 28, 653 (1969).

[19] A. Anders, A structure zone diagram including plasma-based deposition and ion etching, Thin Solid Films. 518 (2010) 4087–4090. http://www.sciencedirect.com/science/article/pii/S0040609009018288.

[20] D.M. Mattox, Surface cleaning in thin film technology, Thin Solid Films. (1978). doi:10.1016/0040-6090(78)90376-0.

[21] G.J. Kominiak, D.M. Mattox, Reactive plasma cleaning of metals, Thin Solid Films. (1977). doi:10.1016/0040-6090(77)90113-4.

[22] M. Köhler, Dry-Etching Methods, in: Etch. Microsyst. Technol., John Wiley & Sons, Ltd, 2007: pp. 111–171. doi:10.1002/9783527613786.ch4.

[23] E. Broitman, Z. Czigány, G. Greczynski, J. Böhlmark, R. Cremer, L. Hultman, Industrial-scale deposition of highly adherent CNx films on steel substrates, Surf. Coatings Technol. 204 (2010) 3349–3357. doi:10.1016/J.SURFCOAT.2010.03.038.

[24] A.P. Ehiasarian, P.E. Hovsepian, L. Hultman, U. Helmersson, Comparison of microstructure and mechanical properties of chromium nitride-based coatings deposited by high power impulse magnetron sputtering and by the combined steered cathodic arc/unbalanced magnetron technique, Thin Solid Films. (2004). doi:10.1016/j.tsf.2003.11.113.

[25] W.-D. Münz, HIPIMS: The new PVD- technology, Vak.Forsch. Prax. 20 (2008) 27.

[26] J.A. Santiago, I. Fernández-Martínez, A. Wennberg, J.M. Molina-Aldareguia, M. Castillo-Rodríguez, T.C. Rojas, J.C. Sánchez-López, M.U. González, J.M. García-Martín, H. Li, V. Bellido-González, M.A. Monclús, R. González-Arrabal, Adhesion enhancement of DLC hard coatings by HiPIMS metal ion etching pretreatment, Surf. Coatings Technol. 349 (2018) 787–796. doi:10.1016/J.SURFCOAT.2018.04.090.

[27] P.E. Hovsepian, A.P. Ehiasarian, A. Deeming, C. Schimpf, Novel TiAlCN/VCN nanoscale multilayer PVD coatings deposited by the combined high-power impulse magnetron sputtering/unbalanced magnetron sputtering (HIPIMS/UBM) technology, Vacuum. 82 (2008) 1312–1317. doi:10.1016/J.VACUUM.2008.03.064.

[28] H.K. Pulker, A.J. Perry, R. Berger, Adhesion, Surf. Technol. 14 (1981) 25–39. doi:10.1016/0376-4583(81)90005-4.

[29] K. Mittal, Adhesion Measurement of Thin Films, Electrocompon. Sci Technol. 3 (1976). doi:10.1155/APEC.3.21.

[30] P.R. Chalker, S.J. Bull, D.S. Rickerby, A review of the methods for the evaluation of coating-substrate adhesion, Mater. Sci. Eng. A. 140 (1991) 583–592. doi:10.1016/0921-5093(91)90482-3.

[31] W. Han, H. Jiao, D. Fox, Scanning Electron Microscopy, in: R. Wang, C. Wang, H. Zhang, J. Tao, X. Bai (Eds.), Prog. Nanoscale Charact. Manip., Springer Singapore, Singapore, 2018: pp. 35–68. doi:10.1007/978-981-13-0454-5_2.

[32] J.I. Goldstein, Scanning electron microscopy and x-ray microanalysis, 3. ed., Kluwer Academic, Plenum Publ., New York, NY [u.a.], 2003.

[33] D.B. Williams, C.B. [VerfasserIn] Carter, Transmission electron microscopy, Plenum Press, New York, NY [u.a.], n.d.

[34] J.M. Thomas, C. Ducati, Transmission Electron Microscopy, in: Charact. Solid Mater. Heterog. Catal., John Wiley & Sons, Ltd, 2012: pp. 655–701. doi:10.1002/9783527645329.ch16.

[35] R. Wang, J. Tao, K. Du, Y. Wang, B. Ge, F. Li, W. Liu, L. Wu, H. Liu, Y. Zhang, Y. Yao, X. Duan, Transmission Electron Microscopy, in: R. Wang, C. Wang, H. Zhang, J. Tao, X. Bai (Eds.), Prog. Nanoscale Charact. Manip., Springer Singapore, Singapore, 2018: pp. 69–203. doi:10.1007/978-981-13-0454-5_3.

[36] H. Moritz, Introduction to Electron Microscopy, Front. Neuroinformatics, 2013, Vol.7. (n.d.).

[37] B. Ge, Scanning Transmission Electron Microscopy (STEM), in: R. Wang, C. Wang, H. Zhang, J. Tao, X. Bai (Eds.), Prog. Nanoscale Charact. Manip., Springer Singapore, Singapore, 2018: pp. 205–254. doi:10.1007/978-981-13-0454-5_4.

[38] R. Schneider, Electron Energy-Loss Spectroscopy (EELS) and Energy-Filtering Transmission Electron Microscopy (EFTEM), in: Surf. Thin Film Anal., John Wiley & Sons, Ltd, 2011: pp. 67–91. doi:10.1002/9783527636921.ch4.

[39] R. Schneider, Energy-Dispersive X-Ray Spectroscopy (EDXS), in: Surf. Thin Film

Anal., John Wiley & Sons, Ltd, 2011: pp. 293–310. doi:10.1002/9783527636921.ch18.

[40] M. Behrens, R. Schlögl, X-Ray Diffraction and Small Angle X-Ray Scattering, in: Charact. Solid Mater. Heterog. Catal., John Wiley & Sons, Ltd, 2012: pp. 609–653. doi:10.1002/9783527645329.ch15.

[41] A. Macková, A. Pratt, Ion/Neutral Probe Techniques, in: Handb. Spectrosc., John Wiley & Sons, Ltd, 2014: pp. 741–778. doi:10.1002/9783527654703.ch19.

[42] H. Hutter, Dynamic Secondary Ion Mass Spectrometry (SIMS), in: Surf. Thin Film Anal., John Wiley & Sons, Ltd, 2011: pp. 141–159. doi:10.1002/9783527636921.ch8.

[43] O. Benka, Elastic Recoil Detection Analysis (ERDA), in: Surf. Thin Film Anal., John Wiley & Sons, Ltd, 2011: pp. 217–227. doi:10.1002/9783527636921.ch13.

[44] Nanovea, Chromatic confocal, (n.d.). http://nanovea.com/chromatic-confocal/ (accessed December 9, 2019).

[45] G.G. Stoney, The Tension of Metallic Films Deposited by Electrolysis, Proc. R. Soc. A Math. Phys. Eng. Sci. 82 (1909) 172–175. doi:10.1098/rspa.1909.0021.

[46] H. Hilbrans, H.-J. Bargel, G. Schulze, Werkstoffkunde, 10th ed., Springer-Verlag, Berlin, Heidelberg, 2008.

[47] W. Weißbach, Werkstoffkunde; Strukturen, Eigenschaften, Prüfung, (2012).

[48] A.C. Fischer-Cripps, Critical review of analysis and interpretation of nanointentation test data, Surf. Coatings Technol. 200 (2006) 4153–4165.

[49] W.C. Oliver, G.M. Pharr, Measurement of hardness and elastic modulus by instrumented indentation: Advances in understanding and refinements to methodology, J. Mater. Res. 19 (2004) 3–20.

[50] A.C. Fischer-Cripps, Nanoindentation, 2nd Ed., Springer-Verlag, New York, 2004.

[51] H. Hirani, Fundamentals of Engineering Tribology with Applications, Cambridge University Press, 2016. doi:10.1017/CBO9781107479975.

[52] Verein Deutscher Ingenieure, VDI Guideline 3198, Vdi-Handb. Für Betriebstechnik. (1992).

[53] Deutsches Institut für Normierung, DIN EN ISO 26443, (2016).

[54] Project Noreia, (n.d.). http://www.project-noreia.at/ (accessed December 10, 2019).

[55] borer Chemie AG, deconex HT 1401, (n.d.). https://www.borer.ch/pdf_files.php?type=prodinfo&file=pdf_files/Industry/english/Product datasheets/deconex_HT_1401_EN.pdf (accessed December 17, 2019).

[56] borer Chemie AG, deconex HT 1170, (n.d.). https://www.borer.ch/pdf_files.php?type=prodinfo&file=pdf_files/Industry/english/Pro

duct datasheets/deconex_HT_1170_EN.pdf (accessed December 17, 2019).

[57] J.F. Ziegler, SRIM, (n.d.). http://www.srim.org/ (accessed January 21, 2020).

[58] J.F. Ziegler, M.D. Ziegler, J.P. Biersack, SRIM – The stopping and range of ions in matter (2010), Nucl. Instruments Methods Phys. Res. Sect. B Beam Interact. with Mater. Atoms. 268 (2010) 1818–1823. doi:10.1016/J.NIMB.2010.02.091.

[59] M. Lattemann, A.P. Ehiasarian, J. Bohlmark, P.Å.O. Persson, U. Helmersson, Investigation of high power impulse magnetron sputtering pretreated interfaces for adhesion enhancement of hard coatings on steel, Surf. Coatings Technol. 200 (2006) 6495–6499. doi:10.1016/J.SURFCOAT.2005.11.082.